



North American Pleistocene Glacial Erosion and Thin Pliocene Regolith Thickness Inferred from Data-Constrained Fully Coupled Ice-Climate-Sediment modelling

Matthew Drew^{1,2} and Lev Tarasov²

¹Department of Earth & Environmental Sciences, Dalhousie University, Halifax, Canada

²Department of Physics & Physical Oceanography, Memorial University of Newfoundland, St John's, Canada

Correspondence: Matthew Drew (mdrew@mun.ca)

Abstract. Beyond the impact of glacial isostatic adjustment, landscape evolution is typically neglected at large scale when considering the basal boundary condition for ice sheet and climate modelling over past glacial cycles. Erosion and changing sediment loads impact bed elevation, land/sea mask, and basal drag. To date, how the above affects past ice sheet evolution is unclear.

5 Constraining the role that Pliocene regolith may have played in Pleistocene glacial cycle variability requires bounds on the amount of regolith preceding those glacial cycles. However, quantitative bounds on regolith thickness at the spatial scale of the glaciated regions of North America are currently absent in the literature.

To address the above, we present an updated sediment production and transport model with dynamically calculated soft sediment mask, isostatic adjustment to dynamical sediment load and bedrock erosion, and a new subglacial hydrology model
10 coupled to the Glacial Systems Model. The coupled model is capable of multi-million year integrations driven only by greenhouse gas concentration and insolation. The model passes a set of verification tests and conserves mass. We assess parametric sensitivity of sediment transport rates.

We compare the final sediment solutions in an ensemble of whole-Pleistocene simulations for a range of initial (Pliocene) regolith thicknesses against multiple estimates for present day drift thickness distribution, Quaternary sediment volume in
15 the Atlantic Ocean, and erosion depth estimates. Consistency of modelling and data constraints requires a Pliocene regolith thickness of less than 50 m.



1 Introduction

During the last three million years, the landscape of North America has been heavily influenced by glacial conditions. A confident determination of the amount of glacial erosion that had occurred over this time interval would strongly aid in deciphering this influence. However, while there are observationally-based estimates for the total amount of sediment removed from North America during this time interval, it is largely unknown what fraction of this material was sourced from glacial erosion of bedrock versus removal of pre-existing Pliocene regolith. Furthermore, it is difficult to infer large scale erosion rates from these estimates as the full area of the catchment (as well as the relative weighting of sourcing within) is generally not well constrained.

25 The mean Pliocene regolith thickness over previously glaciated regions in North America is unknown – broad scale estimates in the literature are based on sparse data (50 m, Clark and Pollard, 1998) or dubious physical reasoning (> 100 m, Willeit et al., 2019). Multiple drill cores in Minnesota show 70 to 184 m of saprolite (in situ, extensively chemically weathered and disintegrated bedrock) underlying glacial deposits Setterholm and Morey (1995). At glacial-sediment-catchment scale, burial dating of early Pleistocene glacial tills indicates the Pliocene regolith must have been thin enough to be removed by 30 the earliest glaciations as later tills had low cosmogenic nuclide concentrations (Balco and Rovey, 2010). Outside glaciated regions, regolith thickness in Australia (sparse glaciation above 1800 m a.s.l., Colhoun and Barrows, 2011) is up to hundreds of metres thick (Wilford et al., 2016). As chemical weathering rates correlate with precipitation (Lebedeva et al., 2010), one could reasonably expect the drier Australian continent to give a lower bound for the amount of regolith overlying the warmer, wetter 35 processes driving chemical weathering and chemical weathering rates may decline poleward due to declining temperatures (?).

Constraining long term erosion rates is necessary for assessing the likelihood of exhumation of long term nuclear waste repositories by glacial action and thus site selection (McKinley and Chapman, 2009). Capable models of sediment transport history allow for more targeted mineral exploration (Klassen and Gubins, 1997) and potentially lowered environmental impact from such campaigns. From an earth system dynamics perspective, such constraint would permit clearer assessment of the role 40 soft sediment processes may have played in the mid-Pleistocene Transition (the Regolith Hypothesis, Clark and Pollard, 1998). To address this, herein we use data-constrained large ensemble modelling to determine such constraints.

Below, we start with an overview of the state of ice sheet sediment modelling and the model used in these experiments, identifying newly added couplings. We then present model verification tests and sensitivity analysis of the sediment transport component. Following these, we describe the available model constraints, inputs, and experimental results and terminate with 45 a discussion and conclusions.

Terminology can prove misleading in inter-disciplinary settings. Throughout the text we take erosion to mean the process of removing material, i.e. transport. We use weathering to mean the physical weathering or disintegration of intact bedrock into unconsolidated sediment, i.e. production, via quarrying and abrasion. When this is done by chemical dissolution we refer to this as chemical weathering.



50 1.1 Current Models of Glacial Sedimentary Processes

Though current paleo ice sheet models can incorporate relevant glaciological processes, climate representation is the largest challenge for long term earth system simulation. For the applicable time scales, full coupling with a general circulation model (GCM) is not feasible. Paleo ice sheet modelling studies therefore make simplifications such as snap shooting output from a GCM, glacial indexing, using lower fidelity earth systems models of intermediate complexity (EMICs), or even simpler energy balance models (EBMs).

The challenge of climate representation is further exacerbated by the uncertainty of atmospheric composition extending back to the beginning of the Pleistocene (or earlier in the case of Pollard and DeConto (2020)). Reliable globally averaged estimates of CO₂ extend back to 800 kyr in the Antarctic ice core record (Bereiter et al., 2015). While the boron isotope proxy record is extending inferences of atmospheric pCO₂ back into the Pleistocene (Chalk et al., 2017), early Pleistocene estimates remain sparse and uncertain (Hönisch et al., 2009).

Glacial sedimentary numerical models have been around for decades (Harbor et al., 1988; Clark and Pollard, 1998; Pollard and DeConto, 2009; Melanson et al., 2013; Ugelvig and Egholm, 2018). However, they have not received the same attention as other aspects of the glacial ice/climate/earth system. For example, there has not been a model intercomparison project as there have been for other important ice sheet processes. These sedimentary models are essentially unconstrained owing to the paucity of quantitative constraint available at the continental scale. The majority of subglacial sediment modelling studies have focused on reproducing ice-catchment scale landscape evolution (*e.g.* (Harbor et al., 1988; Braun et al., 1999; Ugelvig et al., 2016)). Only a scant subset of models have been applied to the scale of continental ice sheets (shown in Table 1).

Numerical continental scale ice sheet models have incorporated subsets of the processes relevant to glacial erosion and at a range of complexities (table 1). At first order, a model must simulate the evolution of ice mass and motion combined with a relationship between motion and sediment transport. Table 1 shows the steady progression of increasing completeness of glacial erosion models over time. Each of these studies must assume initial sediment distribution at simulation start because this quantity is unknown in each case – a further challenge for modelling sedimentary processes.

Simulating removal of regolith along a 1-D flowline profile of the North American ice sheet over the Pleistocene, Clark and Pollard (1998) started with a uniform thickness 50 m of sediment and modelled transport by deformation. They also assumed the entire base of the ice sheet was warm and that effective pressure was close to zero. Clark and Pollard (1998) had to cap ice free areas at 100 m sediment thickness to avoid accumulating around 500 m of sediment at the Southern margin, citing missing non-glacial transport as a short-coming.

Pollard and DeConto (2003) use the same transport model as in Clark and Pollard (1998), supplemented with a sediment production law and applied to a 2-D ice sheet model in Antarctica over 400 kyr. The ice sheet model is asynchronously coupled to a GCM with slab ocean with sufficient temporal resolution to capture obliquity and eccentricity cycles. The model neglects subglacial hydrological processes simulating basal water pressure, thereby requiring the same effective pressure assumption as Clark and Pollard (1998): effective pressure in the sediment layer is only due to sediment weight (water pressure is set = ice sheet overburden). These simulations demonstrate the ability of ice basal action to move tens of metres of sediment from large



Model Reference	Production	Transp	Hyd	Therm	IA	Ice Dyn	Slid Cpl	Dim	Scale
Jenson et al. (1996)	None	Sub	N	N	ice	SIA	N	1D	1500 km/60 kyr
Clark and Pollard (1998)	None	Sub	N	N	ice	SIA	N	1D	2500 km/3 Myr
Dowdeswell and Siegert (1999)	Emp	Emp	N	N	N	SIA	N	2D	
Pollard and DeConto (2003)	Emp	Sub	N	Y	ice	SIA	N	2D	4000 km/400 kyr
Hildes et al. (2004)	Abr/Qr	Eng	N	Y	ice	SIA	N	2D	3500 km/120 kyr
Melanson et al. (2013)	Abr/Qr/Emp	Eng/Sub	Y	Y	ice	SIA	N	2D	3500 km/120 kyr
Pollard and DeConto (2020)	Emp	Sub	N	Y	ice/sed	Hyb	Sed	2D	4000 km/40 Myr
This work	Abr/Qr	Eng/Sub	Y	Y	ice/sed	Hyb	Sed/Hyd	2D	3500 km/2.5 Myr

Table 1. Summary of processes applied in sediment models in the literature. Production is the type of sediment production (Emp is an empirical relation with sliding velocity, Abr is abrasion, Qr is quarrying), Transp is the mode of sediment transport (Sub is subglacial soft sediment deformation, Eng is englacial entrainment and advection), Hyd is whether subglacial hydrology is included, Therm is whether thermodynamics is coupled, IA is the component included in the isostatic adjustment loading (sed refers to the inclusion of sediment loading), Ice Dyn is the ice dynamics used (SIA is shallow ice approximation, Hyb is shallow ice/shallow shelf), Slid Cpl is whether the sediment (Sed) and subglacial hydrology (Hyd) components are coupled into the sliding velocity calculation, Dim is model dimensionality (1D for flowline, 2D for plan view), Scale is the length and spatial scale of the model application. In each case the component complexity is not examined and some components in some models have a more complete treatment than others (e.g. the isostatic adjustment model of Pollard and DeConto (2020) is a local isostatic relaxation model versus the model of Melanson et al. (2013) and this work which is a gravitationally self-consistent global visco-elastic model).



portions of the Antarctic continent in areas which are repeatedly warm based. Transported sediment yields deposits hundreds
85 of metres thick (up to 900 m) after 400 kyr. Interestingly, the authors show large areas which never yield warm based conditions
during the 400 kyr simulation suggesting that pre-glacial sediment may have survived for millions of years.

Pollard and DeConto (2020) extend their effort in Pollard and DeConto (2003) to a continuous simulation over the last 40
Myr. This integration includes improved ice physics and a comparison against seismic observation. Such long model integration
requires low spatial resolution at 80/160 km. The results show sediment production amounts varying 3 orders of magnitude
90 with some channels incised down to 7000 m. Thickness of offshore deposits reach 10 km on the shelf and may be limited by
their imposed surface slope restriction (0.0075 m/m) simulating slumping. They iteratively model pre-glacial topography and
effectively assume 20 m of sediment over the continent and 100 m over marine areas.

Hildes et al. (2004) model sediment movement and generation over the last glacial cycle with a more comprehensive model
(including erosive processes). They assume that the last interglacial sediment distribution is the same as present. Melanson
95 et al. (2013) uses a similar model, integrating ice sheet evolution and sediment processes over the last glacial cycle as well as
assuming present day sediment distribution and topography for last interglacial. Melanson et al. (2013) used the estimates of
total Pleistocene erosion from Bell and Laine (1985) as well as transport distances from the Hudson bay.

Here we present a fully coupled model capable of multi-million year integrations which permits long term simulation of
sedimentary processes such that the results lend themselves to comparison against both the Quaternary sedimentary record
100 and the present day distribution of sediment. For the first time, this model incorporates a fully coupled suite of ice dynamics,
climate, subglacial hydrology and sediment, where the solid earth model incorporates changes in sediment/bedrock load and
the basal velocities depend on the subglacial water pressure and dynamic soft/hard sliding bed mask.

2 Model of Glacial Sedimentation

The sediment model (Melanson, 2012) applied in the Glacial Systems Model (GSM) is designed after that of Hildes (2001).
105 Both employ separate descriptions of abrasion and quarrying for the sediment production part, although Melanson (2012)
provides an optional empirical sediment production as well as a choice between Boulton and Hallet style abrasion whereas
Hildes (2001) uses only Hallet. Hildes (2001) tracks relative hardness of substrate and abrasive, abrasion ceases when the latter
is less than the former, whereas Melanson (2012) assumes the abrading particle is always harder than the substrate. Hildes
(2001) also allows a spatially varying lithology-based calculation of crack growth, and hence of quarrying rates. Hildes et al.
110 (2004) and Melanson (2012) both use estimates of cavitation (from basal water pressure) in the lee side of basal protrusions to
estimate stress regimes and thus quarrying rates. Both models give englacial transport rates through advection, however, Hildes
(2001) omits subglacial transport.

The GSM sediment model equations are detailed in Melanson et al. (2013) but those details are repeated in appendix B for
convenience. Several aspects of this model have been updated since the publication of Melanson et al. (2013): performance
115 improvements by shrinking of subgrid arrays (justified by sensitivity analysis) and array vectorization, improved mass con-
servation through synchronizing all model components in a single time iteration loop, and change to generalized coordinate



reference system on an Arakawa C grid. The sediment model is now coupled to the glacio-isostatic adjustment model of the GSM. The coupling accounts for changing surface load from sediment transport and resultant changes in bed surface elevation (affecting ocean and lake loading). The sediment distribution also dynamically sets the hard/soft bed mask for the basal drag in the ice dynamics solution.

2.1 The Glacial Systems Model

The GSM incorporates a fully coupled system of hybrid SIA/SSA ice physics (Pollard and DeConto, 2012) and 3D ice thermodynamics with local 1D permafrost-resolving bed thermodynamics (Tarasov and Peltier, 2007). We use the grounding line flux approximation of Schoof (2007), subgrid surface mass-balance and ice flow hypsometry parametrization of Le Morzadec et al. (2015), subshelf melt of Lazeroms et al. (2018), surface drainage solver of (Tarasov and Peltier, 2006), and viscoelastic solid earth (Tarasov and Peltier, 1997).

The coupled climate is an ensemble parameter controlled weighting of temperature and precipitation fields from two components: an EBM with 2D geography, non-linear snow and ice albedo feedbacks, and a slab ocean, and a glacial indexing of a set of empirical orthogonal functions (EOFs) extracted from the PMIP I, II, and III modelling results. These modelling projects used multiple ice sheet boundary conditions – ICE4G, ICE5G, ICE6G, Glac1D, and ANU. Of these, ICE4G did not have a major Keewatin Ice Dome. The glacial indexing (interpolation between present day and last glacial maximum conditions) of the EOFs relies both on the height of the simulated Keewatin ice dome from the ice dynamical model and the temperature of the North Atlantic from the EBM slab ocean model. The basal hydrology model is a linked-cavity drainage system coupled to an efficient drainage tunnel solver (Drew and Tarasov, 2023). A more detailed description of the GSM is forthcoming in Tarasov, Hank, and LeCavalier (in prep.).

2.2 Sediment-Isostasy Coupling

We incorporated changes in surface sediment load and bed rock erosion into the loading changes of the solid earth (Tarasov and Peltier, 2004). The current model time to PD bed elevation changes are given by:

$$h_b^t - h_b^{PD} = h_{sed}^t - h_{sed}^{PD} - \text{Ero} + \text{IA} (\text{Ero}, h_{sed}^t - h_{sed}^{PD}) \quad (1)$$

where h_b^* are the bed elevations at current time step and PD, h_{sed}^* are the unconsolidated sediment thicknesses, Ero is the total bedrock thickness which is physically weathered into sediment from quarrying and abrasion over the Pleistocene, and IA is the long term isostatic adjustment due to all of these terms (neglecting shorter term ice and water distribution changes). This isostatic adjustment is calculated on the basis of load changes from the equilibrated (present day plus residual GIA, Tarasov et al., 2012) bed:

$$L_{\text{sed+eros}} = (h_{sed}^{PD} - h_{sed}^t) \frac{\rho_{sed}}{\rho_{ice}} - \text{Ero} \frac{\rho_{rock}}{\rho_{ice}} \quad (2)$$

In fig. D1 we add varying thicknesses of sediment to show the impact on elevation changes of the solid earth surface (not including sediment) due to isostatic adjustment.

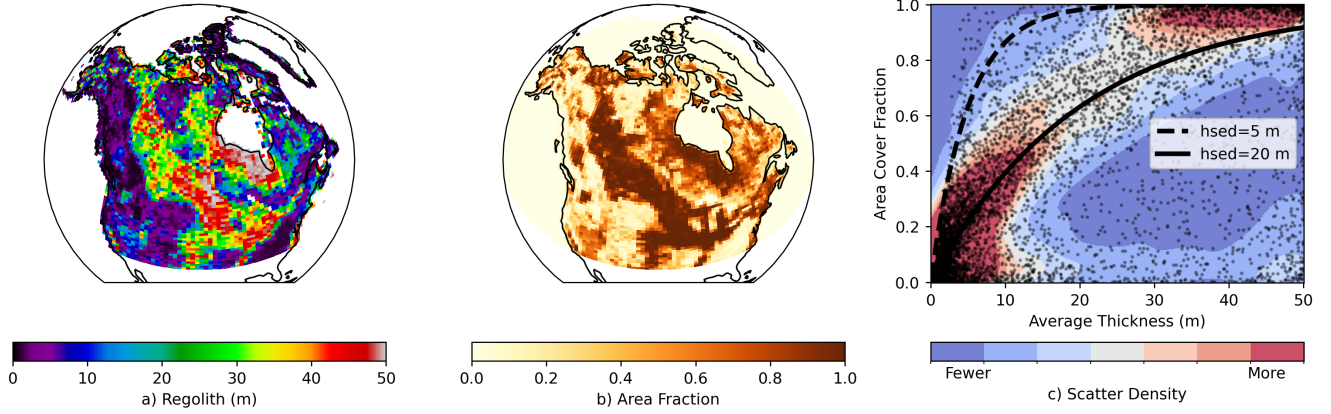


Figure 1. Comparison of present day regolith thickness and area based sediment covered fraction from upscaling the regolith field of Pelletier et al. (2016). Distribution of the upscaled thickness-cover fraction points used for developing a relationship between modelled sediment thickness and soft bed fraction.

2.3 Basal Drag Coupling

The basal velocity is from either a hard or soft bed sliding rule. For the hard bed the basal sliding rule is a fourth power
 150 Weertman sliding law (Cuffey and Paterson, 2010):

$$u_b^{hard} = \frac{c_{hard} f_{Neff} |\tau_b|^3 \tau_b}{N_{eff}} \quad (3)$$

where c_{hard} is a parameterized sliding coefficient which includes a parameterization for basal roughness, f_{Neff} is the effective
 pressure normalization factor, N_{eff} is the effective pressure given by the subglacial hydrology model, and τ_b is the basal drag.
 The basal velocity for soft bedded sliding is similarly a Weertman type sliding law with a parameterized power with integer
 155 values between one and seven.

$$u_b^{soft} = \frac{c_{soft} f_{Neff} |\tau_b|^4 \tau_b}{N_{eff}} \quad (4)$$

with separately parameterized soft sliding coefficient c_{soft} (which also includes a parameterization for basal roughness).

For a soft bed fraction greater than one half, the sliding rule is a soft bed rule, otherwise it is hard. The soft bed fraction is
 calculated with a parameterized relationship with sediment thickness (h_{sed}). To develop this relationship the high resolution
 160 (1 km) sediment dataset of Pelletier et al. (2016) (shown in fig. 1 b)) was upscaled to the GSM North American $1.0 \times 0.5^\circ$
 latitude-longitude grid. The distribution of points in fig. 1 was used to derive a parameterized empirical relationship between
 sediment thickness and soft bed fraction (f_{soft}) to estimate the shielding factor, h_c :

$$f_{soft} = 1 - e^{h_{sed}/h_c} \quad (5)$$

This shielding factor is also used in the quarrying (eqn. B12), abrasion (eqn.), and englacial sediment mixing coefficient
 165 (eqn. ??) relationships.



2.4 Sediment Model Verification Tests

To verify that the model solves the physical equations in § B as intended, a series of model verification tests were performed. The verification strategy was three-fold: symmetric solution given symmetric boundary conditions, convergence to a continuous solution given increasing grid resolution, and conservation of mass. The test bed used for these model solutions was a square root ice sheet topography with coupled subglacial hydrology, sediment, and dynamically calculated basal sliding velocity (from the effective pressure solution of the subglacial hydrology and the driving stress from the square root ice surface).

2.5 Sediment Transport Sensitivity for a Square Root Ice Sheet

Symbol	Description	Distribution	Justification
K_{cond}	hydraulic conductivity of cavity network	$[1e-4, 3e-1]$	(Drew and Tarasov, 2023)
h_r	basal protrusion height	$[0.01, 20]m$	(Drew and Tarasov, 2023)
l_r	basal protrusion wavelength	$[10, 20]m$	(Drew and Tarasov, 2023)
T_{crit}	basal freeze point (PMP rel.)	$[-1, 0]$	Ansatz
$f_{N_{eff}}$	N_{eff} basal sliding term	$[1e4, 2.5e7]$	(Drew and Tarasov, 2023)
HV^*	Vicker hardness bedrock	$[1.5e9, 7e9]$	(Hildes, 2001)
μ^*	Rock-rock friction coef.	$[0.3, 0.85, 10]$	(Byerlee, 1978)
R_{mean}^*	Mean size of grain dist.	$[10^{-4}, 10^{-3}, 10^{-2}]m$	(Boulton, 1979; Haldorsen, 2008; Hubbard and Sharp, 1995)
h_f^*	water film thickness	$[10^{-8}, 10^{-6}, 10^{-4}]m$	(Hubbard and Nienow, 1997; Hallet, 1979)
C_{quar}^*	quarrying coefficient	$[10^{-11}, 10^{-10}, 10^{-9}]Pa^{-1}$	Ansatz, $\propto k_{abr}/HV^{star}$
ζ_b^*	basal roughness	$[0.01, 0.1, 1]$	\propto size erratics (Krabbendam and Glasser, 2011), obstacle size (Weertman, 1957)
n_p^*	quarrying law exponent	$[0.3, 0.5, 1]$	(Cuffey and Paterson, 2010)
h_{sed}^*	shielding factor	$[2, 6, 20]m$	analysis of Fig. 1
ϕ^*	internal friction angle basal sed.	$[20, 22, 24]^\circ$	(Jenson et al., 1995)
n_s^*	rheology exponent of basal sed.	$[1.25, 1.5, 1.75]$	(Jenson et al., 1995)
μ_0^*	Newtownian reference viscosity basal sed.	$[0.1, 5, 100] \times 10^9 Pa s$	(Jenson et al., 1995)
ϕ_p^*	sediment porosity	$[0.3, 0.4, 0.5]$	Ansatz
Z_r^*	thermal resistivity of englacial debris	$[0.23, 0.55, 1.1]mK/W$	(Hildes, 2001; Hallet, 1979)
C_{max}^*	upper bound on sed concentration by vol	$[.85, 0.9, 0.95]$	Ansatz



\tilde{D}^*	prefactor diffusion coefficient	$10^{[-11, -10, -9]} m^2/s$	(Alley and MacAyeal, 1994)
\tilde{z}^*	scale factor for exponential coefficient in D	$[3, 5, 7]m$	Heuristic
C_{crit}^*	critical debris concentration	$[0.3, 0.4, 0.5]$	(Hildes, 2001)

Table 2: Parameters in the GSM sediment model. Those probed with the transport sensitivity analysis in § 2.5 are highlighted in green.

Sensitivity analysis of model behaviour based on uncertainty in the input parameters identifies those parameters which produce the largest variance in the model response phase space. Those producing the widest range in model response would most effectively reduce uncertainty in system behaviour if the parameter uncertainty were reduced. The process of identifying the most important parameters in this sense is called “factor prioritization” (Saltelli et al., 2008). Analyzing model sensitivity to parameter uncertainty also allows identifying those parameters which produce the least amount of variability and, due to a scarcity of computational resources, are not worth probing. The process of identifying those parameters which may be held constant when exploring model response in order to capture system behaviour is called “factor fixing” (Saltelli et al., 2008). In this section we aim to identify those parameters the coupled subglacial hydrology-sediment system which may be fixed and those which are the most important controls on sediment transport.

For most systems, conducting grid search for a 15-dimensional parameter space is unfeasible. Though it depends on model response surface rugosity, a grid search is likely not necessary and low discrepancy sampling methods have been demonstrated to capture phase space variability for some non-linear systems (e.g. see Saltelli (2002)). The most commonly applied sensitivity analyses are variance based methods.

We focus here on sediment transport sensitivity, the parameters controlling sediment production rates are known well enough a priori. Here we use both a variance and a distribution based methods to capture model sensitivity and assess the relative importance of various parameters. These sensitivities are used for selecting ensemble parameters in the following sections and setting the rest to constant values.

Variance based sensitivity indices (S_i) of model response (y) sensitivity to model input (x_i) are built on conditional variances (Saltelli et al., 2008):

$$S_i = \frac{V_{x_i}(E_{x_i}(y|x_i))}{V(y)} \quad (6)$$

which Saltelli et al. (2019) describes as “the expected fractional reduction in the variance of y that would be achieved if factor x_i could be fixed. $S_i = 1$ implies that all of the variance of y is driven by x_i , and hence that fixing it also uniquely determines y .”

Distribution based sensitivity indices are based on a measure of change in the model response distribution from fixing x_i – the difference between the unconditional probability distribution of y and the distribution conditional on a given value of x_i . The Kolmogorov-Smirnov statistic is commonly used as a non-parametric measure of the discrepancy between two distributions

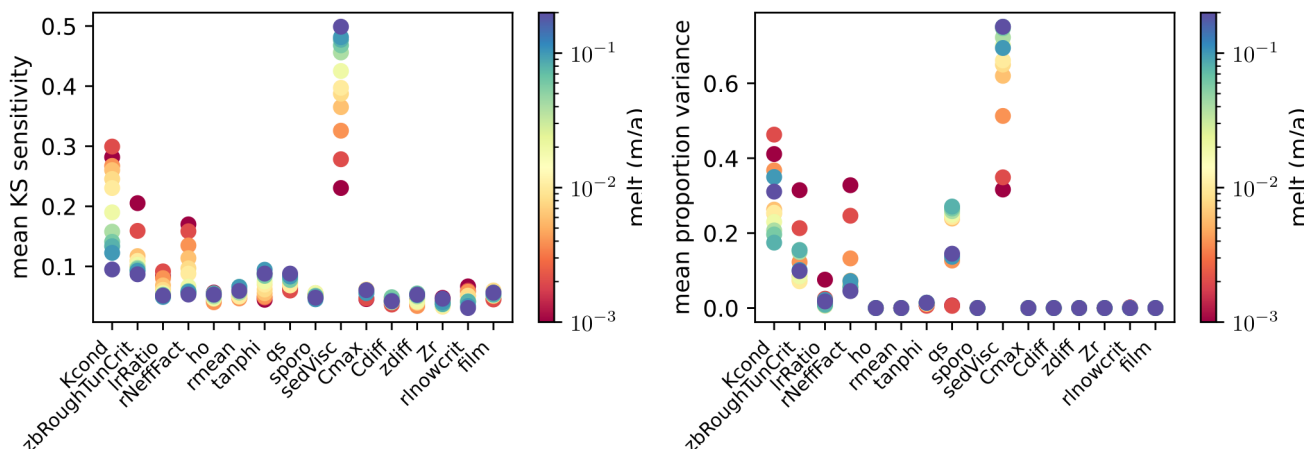


Figure 2. Sediment transport sensitivity to parameters. Mean KS sensitivity is the metric of Pianosi and Wagener (2015), mean proportion variance is the metric of Saltelli et al. (2008).

which Pianosi and Wagener (2015) use to measure the conditional-unconditional difference:

$$S_i = \text{median}_{x_i}(KS(x_i)), \text{ where } KS(x_i) = \max_y |F(y) - F(y|x_i)| \quad (7)$$

where $F(y)$ is the unconditional cumulative distribution function of the model response and $F(y|x_i)$ is the cumulative distribution function which is conditional on selecting $x = x_i$.

For both sensitivity metrics, the amount of sediment transported is most sensitive to the sediment viscosity (fig. 2). The next most important are subglacial hydrology parameters. We therefore assign the subglacial hydrology parameters, sediment viscosity, and the shielding factor (h_c , h_o in fig. 2 to which basal drag and erosion are sensitive) to the ensemble parameter set and assign constant median values to the remaining subglacial sediment model parameters.

3 Constraints

3.1 Present Day Sediment Distribution

To answer what constraint is offered by glaciological constraint and the present day distribution of unconsolidated sediment on pre-glacial sediment thickness, we must first have an estimate for the present day sediment thickness. As uncertain as the Pliocene unconsolidated sediment distribution is, even the present day sediment distribution has large uncertainty. The sediment distribution is most uncertain in Canada where data is sparse. In the United States, relatively dense population gives a wealth of well data whereas broad regions of Canada are sparsely populated. There are some exceptions to this. In Southern Ontario and Quebec, well data, geological surveys and high resolution DEMs give more reliable estimates. Some of the most important areas from a glaciation perspective (e.g. Northern Saskatchewan and Manitoba, Northwest Territories and Nunavut,



Ref.	Region	Source Data
(Taylor, 2023)	Glaciated N. Am.	Geol
(Soller and Garrity, 2018)	Glaciated US East of Rockies	Mult. USGS Databases
(Pelletier et al., 2016)	Global Terrestrial	Wells, Machine Learning
(Shangguan et al., 2017)	Global Terrestrial	Wells, Machine Learning
(Straume et al., 2019)	Global Marine	Seismic & Borehole
(Laske et al., 2013)	Global Terrestrial & Marine	Seismic

Table 3. A summary of large scale datasets available, their geographical coverage, and data sources.

Northern Quebec-Labrador) have no constraint beyond surficial geology mapping (Fulton, 1995) and digital elevation maps from remote sensing (Porter et al., 2018). As such the sediment thickness estimates in these regions are transform functions of those products. Some seismic data are available for reconstructing sediment thickness offshore. However seismic data collection in areas with sea ice cover is difficult and data in the Arctic are sparse (Stashin, 2021).

220 Soller and Garrity (2018) produced a composite map of sediment thickness and bedrock elevation for the glaciated regions of the Northern United States to the East of the Rocky Mountains from many smaller scale regional maps (in fig. 3 d). Naylor et al. (2021) constructed a bedrock elevation map in order to assess present day sediment thickness and bedrock erosion during the Pleistocene. This product synthesized regional maps from many states and provinces in the United States and Canada, subsequently validating the final result against available well data.

225 The sediment distribution by the Canada1Water initiative brought together maps by Soller and Garrity (2018), Parent et al. (2021), Russell et al. (2017), and Smith and Lesk-Winfield (2010). Areas outside these maps were assigned thicknesses based on surficial geologic units from Sur (2014), Karlstrom (1964), and GIS Team National Park Service (1999) with assumed thicknesses for various geologic units in as laid out in table A1.

The offshore areas of Laske et al. (2013) and Straume et al. (2019) are remarkably similar. Indeed, both datasets use seismic
230 methods to estimate the depth of unconsolidated sediment on the oceans seafloors and provide excellent coverage. The issues with using these data to constrain modelled sediment fields are two fold: it is unclear what proportion of those depths are Quaternary aged sediment and it is unclear whether the reported layers which are based on seismic p-wave thresholds correspond to unconsolidated sediment or other units.

Onshore, there is broad agreement on thick sediment coverage in the southern prairies and north-central US and thin sediment
235 over the Rockies. Interestingly, only (Pelletier et al., 2016) gives thick sediment cover of the Hudson Bay Lowlands (south of Hudson Bay). In the Canadian Arctic Archipelago, (Shangguan et al., 2017) and (Pelletier et al., 2016) both show thick sediment over Banks and Victoria Island and moderate sediment over Baffin while (Taylor, 2023) shows thin sediment over the region north of the Arctic Circle as a whole. In terms of total sediment volume, the three reconstructions vary by more than 100% between the most and least capacious: Pelletier et al. (2016) gives 310000 km³, Shangguan et al. (2017) gives 460000
240 km³, and Taylor (2023) gives 200000 km³.

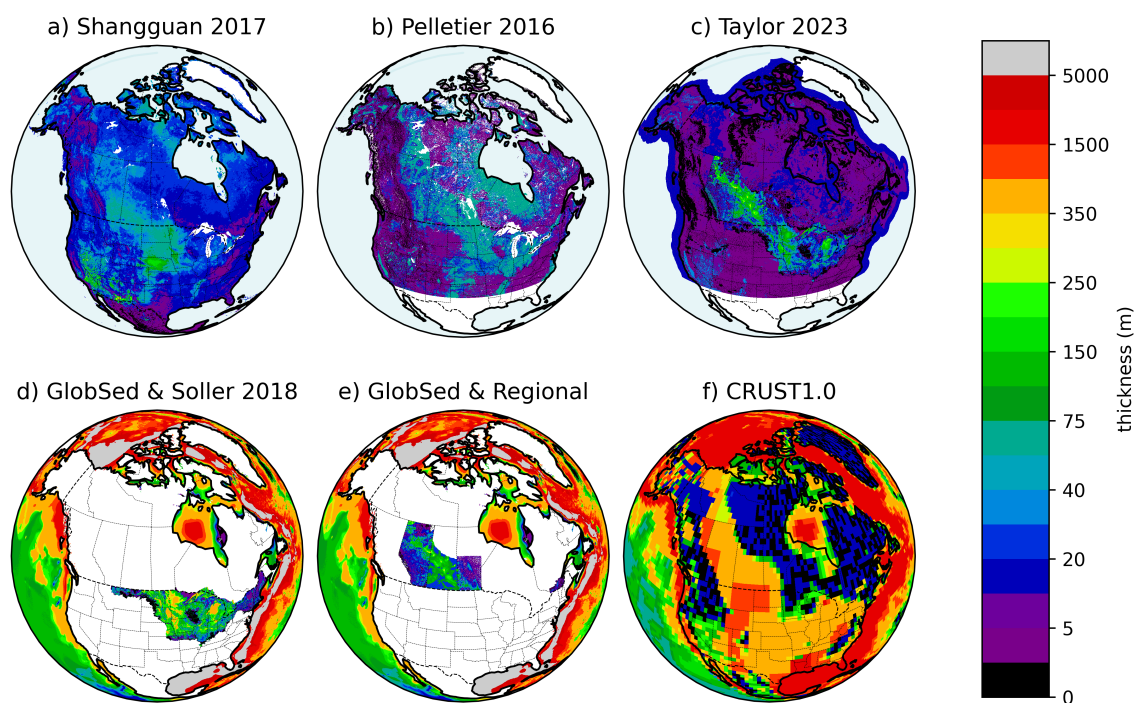


Figure 3. Comparison of various present day unconsolidated surface sediment thicknesses. a) dataset of Shangguan et al. (2017) produced with machine learning methods, b) dataset of Pelletier et al. (2016) produced with empirical relationships from soil profiles and water wells, c) dataset of Taylor (2023) which incorporates many data sources, d) dataset of Soller and Garrity (2018) for the onshore and Straume et al. (2019) for the offshore, e) regional datasets of (from west to east) Atkinson et al. (2020); Fenton et al. (1994); Keller and Matile (2021); Parent et al. (2021) for the onshore and Straume et al. (2019) for the offshore, and f) dataset of Laske et al. (2013). The three datasets (Pelletier et al., 2016; Shangguan et al., 2017; Taylor, 2023) with the best terrestrial coverage were selected for constraining the spatial distribution in the model results. The regional datasets are compared below with bulk volumes for those areas.



Though nearly forty years old, the estimate of Quaternary aged material deposited in the oceans around the domain of the Laurentide ice sheet by Bell and Laine (1985) is still the most comprehensive to date. They detail estimates for the Gulf of Mexico, the west Atlantic, and the Canadian Arctic on the basis of drilling and seismic surveys. Due to the harsh and sensitive environment of the Arctic both drilling and seismic are difficult even today. As such their calculation of Quaternary material for this region has large uncertainties and they state they cannot provide a reliable calculation for this region. Bell and Laine (1985) state that the West Atlantic has excellent seismic coverage and, referring to several studies therein, estimate 1.2×10^6 km³ of Laurentide sourced Quaternary aged sediment in this region. From multiple data sources Bell and Laine (1985) calculate 7.4×10^5 km³ of Quaternary sediment in the Gulf of Mexico. Hay et al. (1989) rejected the Bell and Laine (1985) estimate of Laurentide sourced sediment due to a disagreement on the proportion of Mississippi transported sediment of non-glacial origin. Whereas Bell and Laine (1985) estimate this rate on the basis of the Miocene accumulation rate in the Gulf, Hay et al. (1989) point out that the present day sediment load of the Mississippi river is brought by the Missouri River from the Rockies, not the Laurentide region. Furthermore, because there is no fluvial transport in our model, relating the glacial sediment estimate from (Bell and Laine, 1985) to material glacially transported to the southern margin in our simulations is non-trivial. Because of the above uncertainties, we focus on comparing our model results against the Atlantic region estimate.

3.2 Erosion Estimates

Naylor et al. (2021) estimate 71 metres of bedrock erosion from all sources since the Pliocene in an area encompassing Southern Ontario, Northern US and parts of the Canadian prairies. Ehlers et al. (2006) use apatite (U-Th)/He to estimate hundreds to thousands of metres of bedrock erosion over the Pleistocene. Gulick et al. (2015) use seismic interpretation to reconstruct Pliocene to Pleistocene offshore sedimentation rates. They infer an increase in erosion across the Plio-Pleistocene Transition (PPT) and again during the mid-Pleistocene Transition (MPT). It is not easy to identify the catchment from which these sediments came and so inferring a catchment wide erosion rate is difficult. Though the unstated uncertainties are likely large, the Naylor et al. (2021) erosion estimate is the most useful constraint for modelling North American glacial erosion over the Pleistocene at a continental scale. The bounds on Cordilleran erosion are wide and likely impose less of a constraint on the processes in such a model, meanwhile it is not clear what the precise source region is for the sediment record interpreted by Gulick et al. (2015).

4 Uncertainty in CO₂ Forcing

Proxy data for atmospheric CO₂ concentration prior to coverage by the ice core record (PD-800 ka, Bereiter et al. (2015)) are sparse with wide uncertainty bounds (Hönisch, 2021). Carbon dioxide is well mixed in the atmosphere and the gas is exchanged quickly on paleo timescales at the sea surface. As such that sea surface carbonate chemistry is sensitive to changes in mean atmospheric CO₂. The ¹¹B isotope proxy is sensitive to changes in pH and as such is used as a proxy for atmospheric carbon dioxide (Hönisch et al., 2009). The benefits of this record are its temporal range, estimates are available back to 2.1 Ma. However, the temporal coverage is sparse and not orbitally well-resolved (e.g. Dyez et al., 2018). As such boron isotope

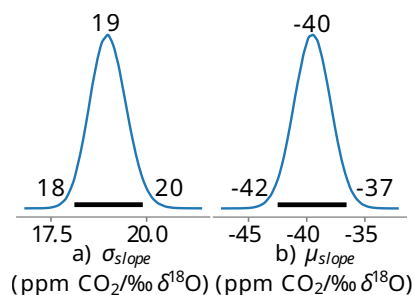


Figure 4. Distribution of the mean and standard deviation of the slope of a linear fit from 800-0 ka between ProbStack (Ahn et al., 2017) and EPICA (Bereiter et al., 2015). The mean value was removed from each dataset prior to fitting. Trends and data can be seen in fig. 4.

records are not sufficient for developing a CO₂ forcing. Other proxies have poorer coverage and larger uncertainties (Willeit et al., 2015; Hönisch, 2021).

275 The benthic $\delta^{18}\text{O}$ climate proxy record has excellent temporal coverage over the Plio-Pleistocene and is sensitive to changes in global temperature, of which CO₂ forms a part of the signal. We adopt the approach of deriving a CO₂ forcing based on this $\delta^{18}\text{O}$ -temperature-CO₂ relationship with the boron isotope record as a validation dataset. As a start point we develop an empirical $\delta^{18}\text{O}$ -CO₂ relationship through regression of the European Project for Ice Coring in Antarctica (EPICA) ice core (Bereiter et al., 2015) and ProbStack (an update to the 5 Myr LR04 stack of 57 benthic records incorporating an additional
280 123 records, better coverage outside the Atlantic Ocean, and improved uncertainty analysis, Ahn et al., 2017) records. We assume a linear relationship between benthic $\delta^{18}\text{O}$ and CO₂ as the analysis of Dyez et al. (2018) does not support higher order terms. We use the PyMC python package for probabilistic programming (Abril-Pla et al., 2023) to develop a generalized linear model through Hamiltonian Monte Carlo sampling (specifically No U-Turns Sampler) and obtain distributions for the linear regression coefficients. First the mean was subtracted from both datasets, then the sampler was run on 16 chains with
285 20000 draws. This yielded distributions for intercept (≈ 0 , left panel fig. 4), mean slope estimate (≈ 40 ppm/‰, centre panel fig. 4), and standard deviation of the slope estimate (≈ 19 ppm/‰, right panel fig. 4). A comparison of the underlying data and the final chosen linear relationship along with a comparison of the output time series and the boron isotope record from data in (Dyez et al., 2018) can be seen in fig. 5. The relationship between oxygen isotopes and carbon dioxide is assumed to change sometime around the MPT and so the slope and intercept coefficients are linearly interpolated to those of the maximum
290 likelihood EPICA-ProbStack linear regression over 1300 to 900 ka. This linear fit persists until EPICA coverage begins at 798 ka. The carbon dioxide time series from the oxygen isotope regression were merged with the carbon dioxide measurements from the EPICA record using a linear weighting over 750 to 798 ka. We test multiple CO₂ forcings on the basis of this distribution, finding that a CO₂/δ¹⁸O slope four standard deviations away from the expected slope and a mean CO₂ of 266 ppm versus the mean EPICA CO₂ of 236 ppm were necessary to attain a target sea level amplitude during the early Pleistocene
295 similar to that of Elderfield et al. (2012) and Rohling et al. (2014). This significant departure (four standard deviations) from the expected regression values of EPICA vs ProbStack is in line with the findings of Dyez et al. (2018) who found that the ice

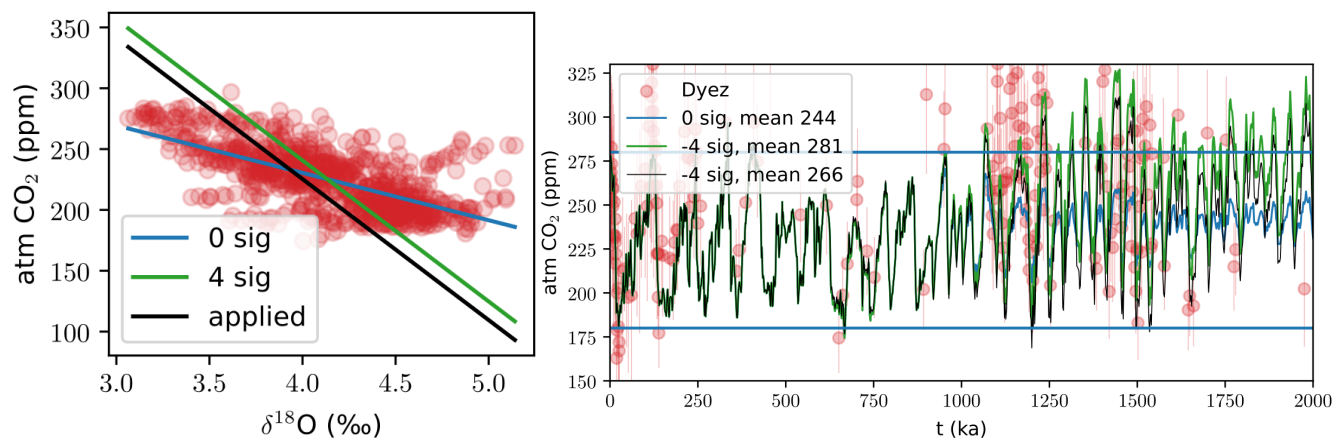


Figure 5. Scatterplot and time series showing the fit of relationships from a linear fit over 800-0 ka between ProbStack (Ahn et al., 2017) and EPICA (Bereiter et al., 2015). Various σ (“sig” in plot legend) based on HMC results in fig. 4.

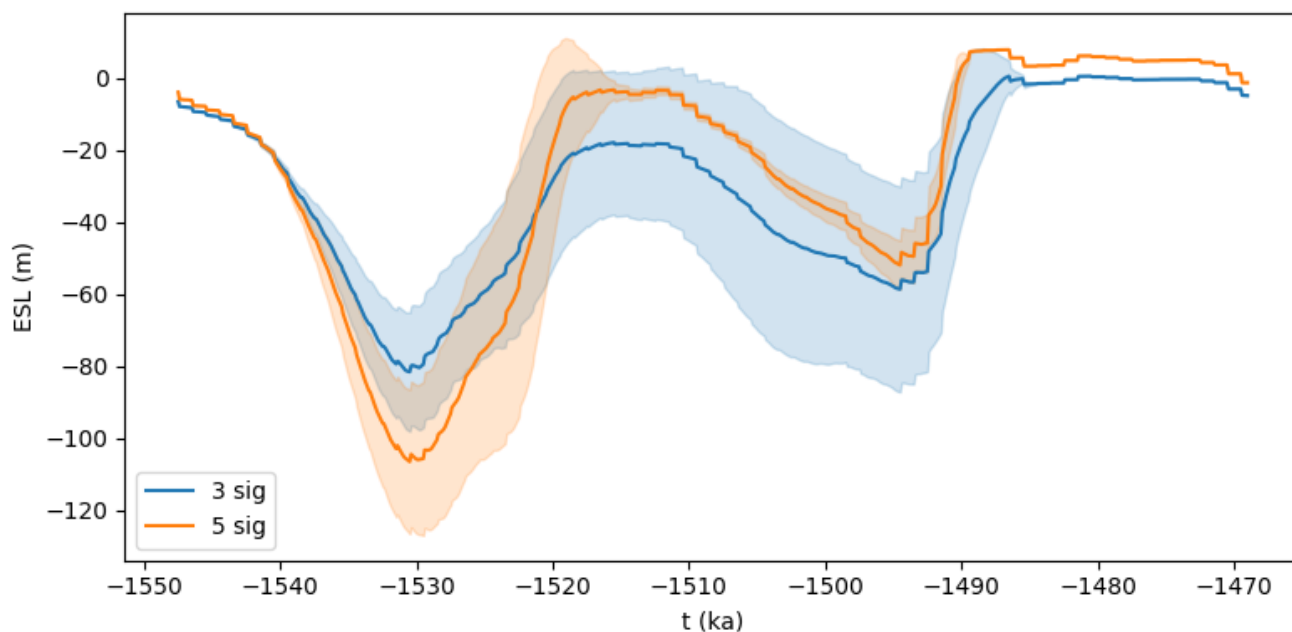


Figure 6. Resulting ensemble mean sea level curves (with one standard deviation shading) for 35 parameter vectors run for CO₂ from ProbStack using a slope three σ and five σ away from the expected value from the distribution shown in fig. 5.

volume-carbon dioxide relationship as approximated by the boron and oxygen isotope records changed significantly across the MPT.



5 Methodology

300 The GSM was run for both the North American Ice Complex (the primary target for our sedimentary study) and the Eurasian Ice Complex (to incorporate a stronger obliquity response). To obtain a set of parameter vectors which reproduce a realistic North American Ice Complex, the model was tuned through several iterations of Latin hypercube sampling for GSM ensemble parameters, simulating the last glacial cycle (-122 ka to present day) and multiple early Pleistocene glacial cycles (MIS 55-45, 1603-1400 ka, an interval with low CO₂ in our forcing), omitting the subglacial hydrology and sediment model components.

305 These sample distributions were then sieved (all runs which lie outside the range for each constraint metric were removed) by bounds on inferred last glacial maximum (LGM) sea level (Spratt and Lisiecki, 2016), deglacial margin chronology (Dyke, 2004), Early Pleistocene sea level amplitude (Rohling et al., 2014; Elderfield et al., 2012), and Early Pleistocene extent (Roy et al., 2004; Balco and Rovey, 2010). These sieved distributions were then fit with a beta distribution and re-sampled with a Latin hypercube for 2 more iterations. This gave a set of basis vectors for the ice dynamic and climate parameters which

310 were then combined with samples for the subglacial hydrology model and re-sieved. This basis vector selection, sampling and combination was done again with the sediment model coupled in.

Simulations with the sieved ensemble parameter vectors were then run for the full Pleistocene continuously (2.58 Myr) with uniform Pliocene regolith distribution initial conditions of 0-120 m thickness with increments of 10 m over both the North American and Eurasian model domains. This range of Pliocene regolith thicknesses covers the mean material removal over

315 glaciated North America estimated by Bell and Laine (1985).

6 Results

6.1 Data-Model Comparison

Here we compare model results with the present day sediment distribution reconstructions by Taylor (2023), Shangguan et al. (2017), and Pelletier et al. (2016). Each data set was interpolated to the GSM model grid for comparison against model results

320 (`cdo remapbil`, Schulzweida, 2023). The data of Pelletier et al. (2016) were extrapolated over missing data in lakes and ocean areas then upsampled (`cdo fillmiss` Schulzweida, 2023). Prior to comparison, all three data sets were masked to the same coverage as Shangguan et al. (2017) (no coverage over ocean areas, great lakes and major lakes in the Canadian Prairies). The max and min across the three data sets for each cell was extracted and used as the bounds for misfit scoring. Modelled thicknesses which lie within these maximum and minimum bounds were assigned zero misfit, outside this range the difference

325 with the closest bound was used. In Fig. 7 a) we examine the mean L1 norm misfit with respect to these bounds.

Taken as a whole, these results presented in Fig. 7 and further examined in Fig. 8 to incorporate glaciological controls indicate that Pliocene regolith thicknesses were likely less than 50 m. Fig. 7 shows that the match between simulated and observed present day sediment distribution gets progressively worse as the regolith scenarios thicken. This may be the result of underestimating the thickest sediment packages by reconstruction schemes which extrapolate thin sediment coverage outside

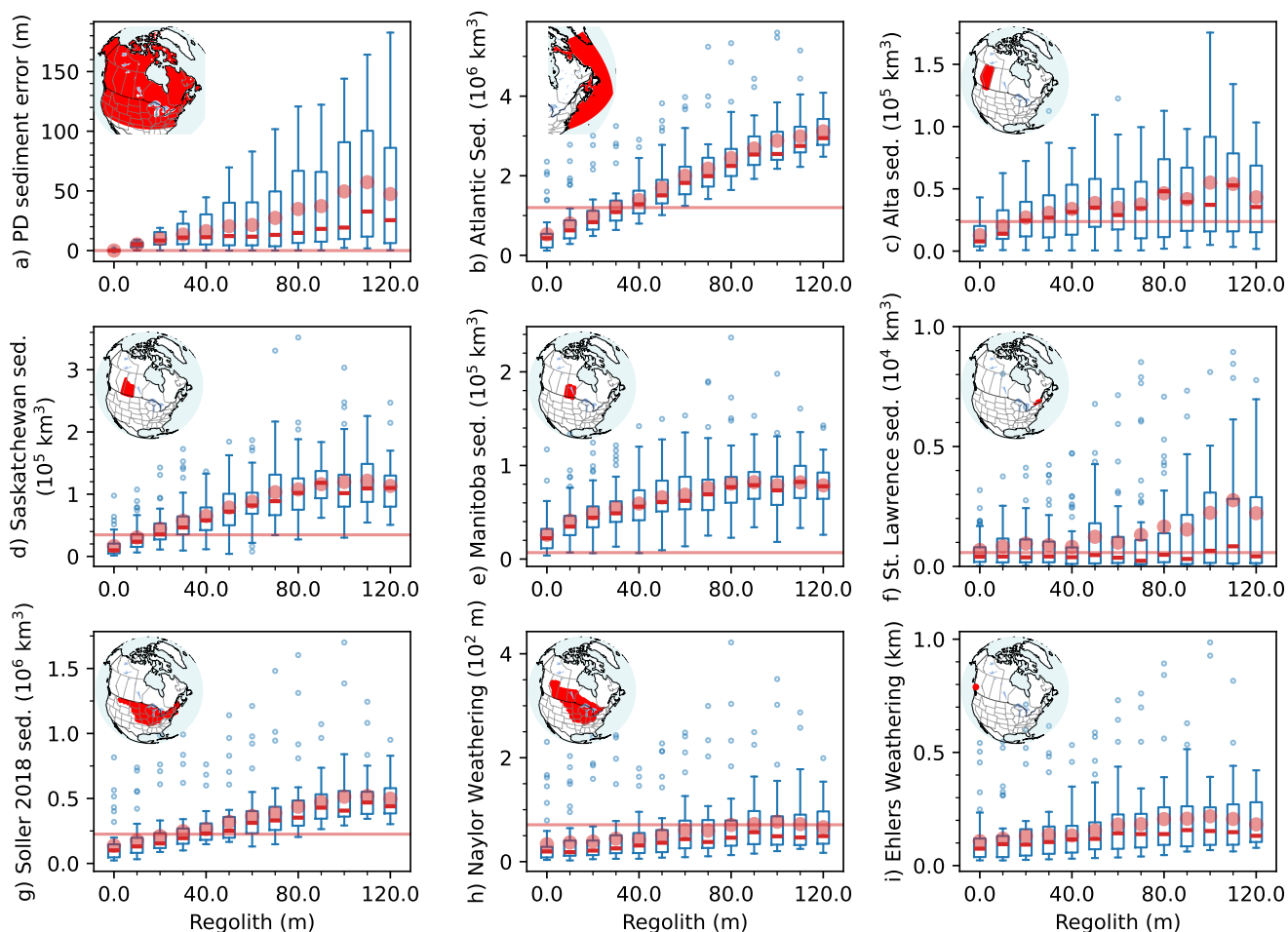


Figure 7. Comparison of observed present day sediment volumes and erosion thickness estimates against modelled quantities for varying levels of starting sediment thickness (regolith scenarios). The red dots indicate mean and short red lines indicate median for each regolith scenario. Panel a) shows the L1 misfit with the estimated present day distribution of sediment as detailed in sec. 6. In panel b) the Bell and Laine (1985) estimate for total Quaternary sediment deposited from North America into the Atlantic is shown by a horizontal red line. Panel c) shows modelled and observed sediment volume for Alberta by Atkinson et al. (2020), d) for Saskatchewan by Fenton et al. (1994), e) for Manitoba by Keller and Matile (2021), and f) for the St. Lawrence estuary by Parent et al. (2021). Panel g) compares the modelled and observed sediment volume for the formerly glaciated region of the United States East of The Rockies by Soller and Garrity (2018). In panel h) the Naylor et al. (2021) estimate for mean bedrock erosion depth (71 m) in their study area is shown by a horizontal red line. Panel i) is the erosion depths in the study location of Ehlers et al. (2006) where bounds on observed values are 100's to 1000's of metres.



330 areas of better data coverage on the basis of surficial geology (Taylor, 2023) or change in relationship between input data and
sediment thickness further North due to a change in surface processes (Pelletier et al., 2016; Shangguan et al., 2017).

Regional datasets were collected where available at scales comparable to that of the model. This covered the prairies of
Western Canada, the St Lawrence valley and the Atlantic Basin estimate of Bell and Laine (1985). We compare the model
results against these regional datasets from west to east. Bulk volume estimates are less prone to error than the individual
335 locations and so are a better target for data-model comparison. For all regions, the modelled bulk sediment volume increases
with starting regolith thickness – though the trend is more linear for some regions than others.

The amount of sediment exported to the Atlantic basin increases roughly linearly with increasing amounts of pre-glacial
regolith. This indicates that, in this large depo-zone for a significant portion of the Laurentide catchment, the North American
Ice Complex does not suffer from shielding of bedrock from weathering by regolith cover. The ice sheet is able to evacuate
340 sufficient sediment such that erosion can continue to produce nearly the same amount of sediment in the thicker regolith
scenarios. The mean and median estimates for the 30 and 40 m ensembles in fig. 7 b) agrees remarkably well with the amount
of sediment transported to the North American Atlantic sector estimated by Bell and Laine (1985). However this estimate
carries large uncertainty and both the 10 m and 50 m ensemble median values lie within 50% uncertainty bounds.

The Alberta drift thickness dataset is the isopach for the land surface to top of bedrock difference (Atkinson et al., 2020). As
345 such, errors in the bedrock elevation surface will propagate into the drift thickness dataset. This bedrock elevation surface was
produced with machine learning techniques which used training and validation data from boreholes and 39 terrain and geologic
input datasets. The sediment volume increases linearly at first but becomes erratic after about 50 m of regolith, possibly due to
the dual influence of the Cordilleran and Laurentide ice sheet not present in the other regions. Here the observed bulk sediment
volume stays within the interquartile range for all ensembles except the 0 m one. The trend in ensemble median values is
350 closest to this observed value between 20-40 m of regolith.

Fenton et al. (1994) reconstructed the drift thickness in Southern Saskatchewan. In this region the modelled sediment volume
increases linearly out to about 90 m and then flattens off indicating significant shielding of the bedrock from weathering. The
observed bulk sediment volume lies within the modelled interquartile range for starting regolith thicknesses from 10 to 20 m.

The Southern Manitoba region here appears to be a bit of an outlier among the prairie provinces. Sediment volumes recon-
355 structed by Keller and Matile (2021) from multiple borehole databases are five times lesser in Southern Manitoba than those
of (Fenton et al., 1994) in Southern Saskatchewan (though the areas are comparable). The lower Manitoba sediment volume
is not reflected in the model results which give similar volumes in both provinces. The sub-linear trend in sediment volume
with increasing regolith thickness indicates that bedrock shielding may be more significant here than in other sectors of the ice
sheet. This may result from insufficient transport capacity to denude the bedrock or some significant process absent the model.
360 In this region none of the regolith scenarios agree with the observation.

The till thickness reconstruction of Parent et al. (2021) collated geological models for multiple subregions within the study
area based on borehole and geophysical data, filling gaps between them. Examining the established stratigraphy in the area
Parent et al. (2021) describe multiple glacial advances within the last glacial cycle alone – the Quaternary record in this area has
been repeatedly wiped clean. Comparing the modelled sediment thickness in this area with their till volume reflects this – the



365 ensemble median values largely agree with the observed volume regardless of regolith scenario. The fast flowing ice regime here has enough transport capacity to denude the bedrock. Interestingly, this is the only region with appreciable departure of mean from median modelled sediment volumes – the distributions get progressively more skewed with thicker regolith scenarios.

Fig. 7 g) compares the modelled sediment with the reconstruction by Soller and Garrity (2018) for the previously glaciated United States areas east of the Rockies. This reconstruction was based on several geologic databases detailed within their publication. Sediment volumes increase roughly linearly out to the 90 m regolith scenario. The 20-50 m regolith scenarios have interquartile ranges which envelope the observed sediment volume.

The bedrock removal reconstruction of Naylor et al. (2021) poses an upper bound on physical weathering of the bed by glacial processes as that reconstruction does not separate out chemical, biological, and other physical weathering processes which contribute to the production of sediments (Goudie and Viles, 2012). The median bedrock erosion values in Fig. 7 h) are below this estimate for all regolith scenarios and any trend in the amount of bedrock quarried or abraded is small or non-existent. This indicates that for the majority of the Southern Laurentide domain, the ice sheet is able to remove the debris produced by quarrying and abrasion and bedrock shielding is not a limiting factor.

In Fig. 7 i) we show the bedrock removal thickness over the study area of Ehlers et al. (2006). They inferred large erosion bounds in their study area of 100's to 1000's m and, as such, their bounds do not pose a constraint on these results. The wide distribution within each ensemble also shows this spread. Whereas the wide bounds on erosion depth inferred by Ehlers et al. (2006) is the result of both methodological uncertainty from thermochronometry and likely wide range in basal thermal regime in rough terrain, the distribution in each ensemble is due to parametric uncertainty. This illustrates the challenge of reconciling the scales of a typical geologic study area and ice sheet modelling.

385 6.1.1 Regolith Thickness Inferred by Applying Constraint Bounds to Model Runs

Here we discard runs which lie outside the plausible range of earth systems histories on the basis of the uncertainty bounds for glaciological and sedimentary constraints – a process referred to as sieving. The sieve was designed based on sensitivity of the inferred Pliocene regolith bounds to each constraint, the plausible uncertainty range for that constraint, and uncertainty in modelled earth system evolution due imperfect process representation, initial and boundary conditions, and scale. For example, while the timing of the removal of the ice dam between the Hudson Bay and Atlantic ocean is well constrained (Alley and Agustsdottir, 2005; Thomas et al., 2007; Matero et al., 2017), models aiming to capture the overall features of the full Pleistocene glacial cycles will perform more poorly at the millennial scale. As such the runs outside the (loose) 4.1 to 12.3 kyr range were discarded.

The next constraints applied to the ensembles control for extent of the North American ice sheet: scoring against the deglacial margin chronologies of Dyke (2004) and Dalton et al. (2020) and the early and late Pleistocene most southerly tills of Roy et al. (2004) and Balco and Rovey (2010). For these, runs outperforming the ensemble median margin score and those with early Pleistocene minimum latitude of ice between 38 and 43 ° N both before and after 1 Ma were kept. The next set of controls was early Pleistocene and LGM sea level. LGM sea level is generally accepted to have been between 125 to 140 m below

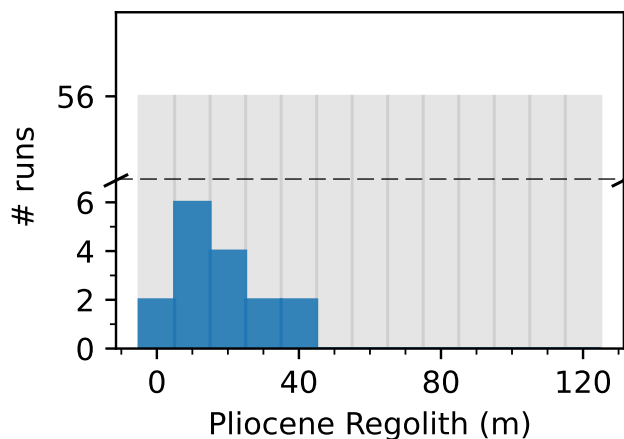


Figure 8. Sieved Pliocene regolith thickness distribution (blue) with full ensemble Pliocene regolith thickness distribution (greyed-out, constant 56 runs per level).

present (Austermann et al. (130 m 2013), Lambeck et al. (130-140 m 2014), Yokoyama et al. (125-130 m 2018). Sea level
400 in the GSM is calculated using a scale factor to convert ice volume to barostatic sea level change and is based on the present
day ocean area. Furthermore, only the North American and Eurasian ice sheets are modelled here – for the remaining bodies
of terrestrial ice a scale factor is applied. Due to differences in how sea level is calculated here and the calculations from the
glacial isostatic adjustment (GIA) community stated above and additional allowance for the temporal scales modelled here, we
discard those runs outside of 100 to 150 m sea level drop at LGM. In the early Pleistocene (older than 1 Ma) we take rough
405 sea level from Elderfield et al. (2012) and Rohling et al. (2014). Given the wide uncertainties in those records (the two records
are occasionally anti-phase for example), we discard runs with an early Pleistocene sea level minimum outside of 50 and 120
m. The number of runs passing the sieve is not very sensitive to these bounds and changing them by 10 m only changes the
number of runs passing the sieve by 1.

Following the above glaciological controls, we apply the sedimentary constraints. The average removed bedrock thickness
410 of ≈ 70 m by Naylor et al. (2021) carries uncertainties which are difficult to assess as this is based on geomorphological
interpretation of the mapped bedrock and reconstruction of the isostatically adjusted Pliocene landscape. Errors in the bedrock
mapping depend on data coverage and any systematic biases thereof – this could introduce errors in bedrock elevation we
estimate to be on the order of 10 m. Interpretation of this surface to produce a Pliocene bedrock surface may compound these
errors five or ten fold. As such we assume an order of magnitude change for the lower bound of average bedrock removal – 7
415 m. The sieve is not sensitive to an upper bound beyond their estimate and so we take 70 m for this value.

As the Alberta (Atkinson et al., 2020), Saskatchewan (Fenton et al., 1994), and northern US (?) data sets cover large areas
in locations with excellent borehole coverage due to their natural resource industries, it is very unlikely that the volume of
sediment in these areas could be off by more than a factor 2. We take half to twice these volumes as bounds. The St Lawrence

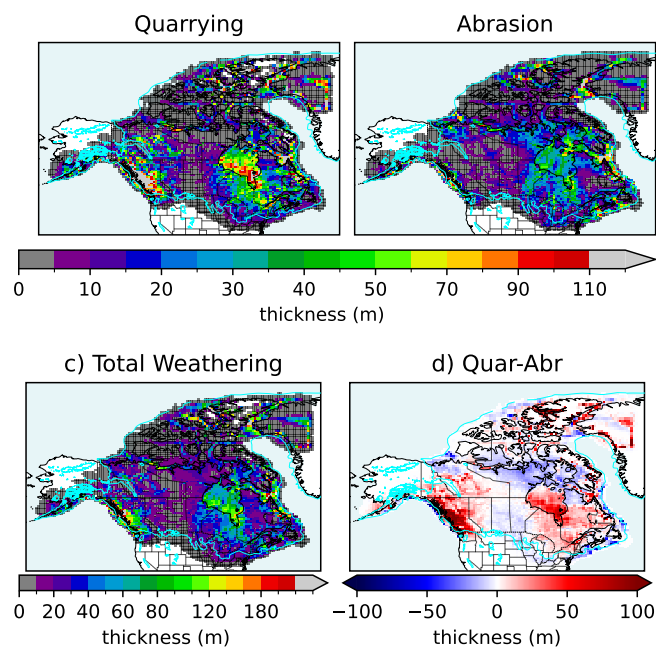


Figure 9. Mean depth of bedrock weathered over the Pleistocene due to a) quarrying and b) abrasion. Total weathering thickness is shown in c) and the difference between quarrying and abrasion is shown in d).

dataset of (Parent et al., 2021) covers a smaller region and so the comparison with the GSM scale is more tenuous. As such we apply bounds of one third to three times this sediment volume. Finally, while the estimate of (Bell and Laine, 1985) covers a large area like the first three datasets, it relies on seismic data which carries uncertainties in the velocity models used to convert travel time to depth, the interpretation, and the acquisition and processing steps. As such we widen these uncertainty bounds further taken one quarter to four fold their sediment volume.

Applying all of these bounds in parallel to sieve the ensemble brings the number of runs from 728 to 16 (cf Fig. 8). The initial regolith thicknesses for the latter surviving subset of runs spans 0 to 40 m, while no runs with 50 m initial sediment thickness passed the sieving. This suggests that the mean Pliocene regolith was less than 50 m thick with no lower bound inferrable from the above analysis.

6.2 Quarrying, Abrasion, and Overall Physical Weathering

Broadly, modelled quarrying and abrasion thickness shown in Fig. 9 is at similar scales and active in similar areas. Weathering by both modes is high in the channels of the Canadian Arctic Archipelago and Hudson Strait and low on the islands. Since the bedrock erodibility is constant, this illustrates the importance of topography and ice stream formation for weathering efficacy. Quarrying is particularly effective in the Rockies where variable topography encourages streaming and melt-water formation

due to basal friction. Quarrying is also dominant in the Hudson Bay and Northwest Territories. Abrasion dominates in northeast mainland Nunavut, along the margin of the Quebec-Labrador sector, and other marine margins.

435 7 Discussion & Conclusions

It is thought that denudation of the Canadian shield occurred at some point following the intensification of Northern Hemispheric glaciation, removing a covering of regolith developed during the Pliocene or earlier (White, 1972; Clark and Pollard, 1998; Willeit et al., 2019). However, when sediment model parameters are tuned for agreement with the bedrock erosion depth estimate of Naylor et al. (2021), the sediment areal coverage over North America does not decrease much or in some cases
440 actually increases. There are four potential reasons for this: 1. the sediment transport parameters should be tuned for a more transportive ice sheet, 2. the unstated uncertainties in bedrock erosion estimates of (Naylor et al., 2021) are large and lower values may be correct, 3. the missing fluvial, glacio-fluvial, and hillslope processes may be more important than assumed, and 4. there was little regolith cover in the Pliocene. The main sediment transport parameter is the sediment viscosity in the soft sediment deformation rheology relationship eq. ???. While this parameter is largely unconstrained, decreasing the sediment
445 viscosity results in peak sediment velocities which depart from observed sliding velocities in contemporary ice sheets. The uncertainties in the present day bedrock surface depth map of Naylor et al. (2021) are not stated and are likely far less than their Pliocene surface geomorphological reconstruction, the two inputs to their bedrock erosion estimate. It is difficult to assess how large these uncertainties are without an intimate understanding of the inputs and workflow. A detailed uncertainty assessment of these reconstructions would strongly facilitate interpretation and usability.

450 The fluvial role in North American sediment coverage following 2.58 Myr of Pleistocene glaciation remains to be quantified. Koppes and Montgomery (2009) point out that where sediment is mobilized by recent disturbance, a condition which a recent deglaciation likely satisfies, fluvial transport can increase “dramatically.” Furthermore, the large amount of water availability during deglaciation and glacial lake drainage events may also increase this effect. Future work to encapsulate sediment transport due to glacial lake drainage events, glacio-fluvial transport, and interglacial fluvial and hill slope transport in a model similar to
455 that presented here would help assess to what degree those processes can increase the amount of sediment transported during the Pleistocene. During interglacials chemical weathering could weaken bedrock and produce more quantities of regolith throughout the Pleistocene requiring even greater transport. Of course it is also possible that there was not enough Pliocene regolith to require an increased transport capacity to match the present day observation. If the change in North American hard bedded area across the Pleistocene was not significant, this would refute the regolith hypothesis for the mid-Pleistocene
460 Transition.

Our understanding of the change in sediment coverage over the Pleistocene can be made more confident by quantifying the amount of Pleistocene aged sediment in significant depositional basins. Large scale geomorphological interpretation of large terrestrial deposits could help distinguish between the roles of glacial versus (glacio)fluvial transport. Notable terrestrial depositional basins for glacial sediment simulated by the model are: the area at the southern end of the glaciated Rocky and
465 Coastal Mountains, southern margin tills in north-central USA, Western Canadian Sedimentary Basin, and the Hudson Bay

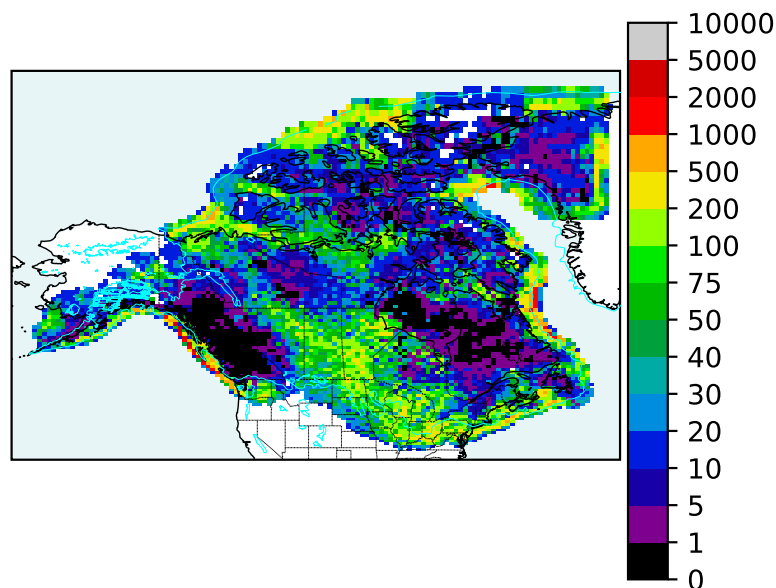


Figure 10. Mean ending sediment distribution across all parameter vectors and initial sediment thicknesses.

Lowlands. Pelletier et al. (2016) shows a thick sediment package in the Hudson Bay Lowlands whereas Taylor (2023) and (Shangguan et al., 2017) do not. We do not know of any reliable sediment volume constraint currently available in the Hudson Bay Lowlands.

The regional sediment volumes from the datasets of Fenton et al. (1994); Soller and Garrity (2018); Atkinson et al. (2020); Parent et al. (2021) provide important constraint where the present day sediment distributions of Pelletier et al. (2016); Shangguan et al. (2017); Taylor (2023) fall short. The sediment volume over southern Manitoba (Keller and Matile, 2021) is an outlier when considered alongside the other regional datasets. When applied in tandem with glaciological constraints as detailed in Sec. 6.1.1 these suggest a Pliocene regolith thickness of less than 50 m.

Total sediment production is largely insensitive to the amount of starting sediment tested here (fig. 9, E1), though a small trend does emerge when examining sediment production amounts as in fig. 7. Fig. 7 shows good agreement between the median value of Atlantic marine sediment in the model and the estimate of Bell and Laine (1985) at 20 m initial sediment thickness. Median modelled bedrock erosion in the reconstruction area of Naylor et al. (2021) lies below their estimate of ≈ 70 m for all initial regolith thicknesses. The Ehlers site erosion results are all in range of the wide bounds by Ehlers et al. (2006). The simulations with less starting sediment score better against the present day distribution of sediment. Additional estimates on the spatial distribution of Pleistocene erosion depth at a catchment scale in more northern areas (e.g. Nunavut) would provide good constraint for the Pleistocene sediment budget and help improve understanding of glacial erosion processes. For example, estimates of erosion from terrestrial cosmogenic nuclide concentrations in till can be used to estimate mean catchment erosion rates at a scale comparable to ice sheet modelling (Staiger et al., 2006).



Quarried and abraded thicknesses are similar in magnitude and location with a few difference. Fig. 9 d) shows the quarrying-
485 abrasion difference ($\int \dot{Q}dt - \int \dot{A}dt$). This highlights that quarrying is the dominant mode of physical weathering in the
Cordillera, the Hudson Bay and parts of Quebec, and the fjords around Ellesmere island. Topographic troughs facilitate ice
streaming and melt water production giving high subglacial cavity growth rates and thus quarrying. Also, variable topography
results in higher basal strain heating and increased meltwater production, which explains the dominance of quarrying in the
Cordillera.

490 The modelled weathered thickness in Greely Fjord ranges between 100-400 m where bathymetry ranges 200 at the head 500
at the mouth (all bathymetry numbers from Group, 2023). In Nansen Sound the modelled weathered thickness range from 250
to more than 400 m and the present day bathymetry is around 800 m deep. In the Laurentian channel area – which is between
80 and 450 m below its flanks – the model gives 100-140 m of weathering. As this feature is below the resolution of the model
the local weathering could increase at higher resolution.

495 Interestingly the physically weathered thickness in the Hudson Bay matches the bathymetry there at present day. The weath-
ered thickness ranges 80 to 200 m and the bathymetry range 60 to 250 m with more weathered areas correlating the deeper
parts of the bay. This supports the hypothesis that prior to glaciation the Hudson Bay region was sub-aerial and perhaps a large
river system which was subsequently excavated during glaciation (the Bell River Hypothesis, Corradino et al., 2021; Sears and
Beranek, 2022). Connecting these modelled weathering rates with topographic lows presupposes increased pre-glacial erodi-
500 bility in these areas as the present day topography was used to simulate the weathering and topographic lows beget topographic
lows. Nevertheless, for the Hudson Bay at least, it is a priori plausible that this area was more erodible as it is underlain by
softer carbonates (Hanna et al., 2018). These differences in bedrock erodibility may be seen as physiographic character which
encourages bedrock weathering or as material weakness within the rock due to lithology, fracture, or jointing (e.g. Hooyer
et al., 2012).

505 In this model, most of the sediment is transported to marine areas (see fig. 10) An exploration program (or re-analysis of
past programs) over a few offshore basins would provide good constraint to the Quaternary sediment budget. Perhaps the most
significant and accessible location for sediment budget constraint is the Saglek Basin area at the mouth of Hudson Strait. The
Saglek basin is distal from large present day fluvial systems and its Pleistocene sediment volume is probably dominated by
ice stream transport. This area has been of interest for oil & gas exploration in the past and there are several wells and 2D
510 seismic lines in the area (Jauer and Budkewitsch, 2010). This basin would also be the deltaic depocenter for the hypothesized
Bell River which is supposed to have carried sediment from large parts of North America across a terrestrial Hudson Bay prior
to glaciation. This far-flung dispersion is support by recent detrital zircon work showing some of the pre-glacial sediment in
the Saglek basin came from the Colorado Plateau (Sears and Beranek, 2022). Similarly, the Laurentian Channel and Scotian
shelf have been targeted for exploration with existing data coverage. Additional areas include the north end of Baffin Bay and
515 Canada Basin – though exploration in Canada Basin in particular has proved especially difficult (Stashin, 2021).

Based on the discussion above, we would single out two desired model inputs to make the basal processes representations
more realistic. Rougher terrains will have more bedrock rising above the unconsolidated sediment fill – the hard bedded area
calculation should account not only for the mean thickness of sediment but for topographic roughness as well. High resolution



(2 m) digital elevation models (DEMs) are available which would allow roughness calculations at the relevant several metre
520 scales (Porter et al., 2018). This would also allow incorporating basal roughness in the sediment and subglacial hydrology
models as a field from DEMs than a spatially uniform parameter. It is not clear, however, what measure of basal roughness
(e.g. standard deviation, slope, power spectra, etc.) would be most applicable. Bedrock erodibility likely varies spatially as well,
whereas in the model it is currently treated as a uniform uncertainty parameter. Quarrying has been shown to be controlled by
525 of erodibility in the respective modes based off lithology and other attributes would be a major improvement.



Code and data availability. Data sets and code will be made available upon final acceptance for publication. We plan on providing sediment cover and bed elevation anomaly during interglacials for a range of parameterizations and welcome reasonable suggestions for additional outputs.

Appendix A: Present Day Sediment Estimates

Unit	Description	Thickness (m)
I	Glacier ice	not used
O	Organic > 2 m	3
E	Eolian	3
Cv	Colluvial veneer	1
C	Colluvial seds, undif	4
A	Alluvial seds, undif	4
Ln	Lacustrine (littoral, nearshore)*below modern lakes	5
Lo	Lacustrine (offshore)*below modern lakes	10
Mn	Marine (littoral, nearshore)*below modern seas	5
Mo	Marine (offshore)*below modern seas	10
GMn	Glaciomarine and marine (littoral, nearshore)	5
GMv	Glaciomarine and marine (veneer)	1
GMo	Glaciomarine and marine (offshore)	10
GLn	Glaciolacustrine and lacustrine (littoral, nearshore)	5
GLo	Glaciolacustrine and lacustrine (offshore)	10
GFp	Glaciofluvial seds (outwash plain)	10
GFc	Glaciofluvial seds (ice-contact)	25
Tv	Glacial seds (till veneer)	1
Tb	Glacial seds (till blanket)	7
Th	Glacial seds (hummocky till)	10
Tm	Glacial seds (moraine complex)	35
Wv	Weathered bedrock (regolith veneer)	1
W	Weathered bedrock (regolith, undiff)	3
V	Bedrock (Quaternary volcanic rocks and deposits)	0
R	Bedrock, undiff (> 75% outcrop)	0

Table A1. Assumed sediment thicknesses by surficial geologic unit used by Taylor (2023) for reconstructing the present day sediment thickness over North America were direct observations were lacking (outside the study areas of Soller and Garrity (2018); Parent et al. (2021); Russell et al. (2017); Smith and Lesk-Winfield (2010)).



530 Appendix B: Description

The sediment model applied in the GSM is designed after that of Hildes (2001). Both employ separate descriptions of abrasion and quarrying for the erosive part, although Melanson (2012) also provides an optional empirical erosion as well as a choice between Boulton and Hallet style erosion whereas Hildes (2001) uses only Hallet. Hildes (2001) input a map of substrate lithology and track the distribution of clast lithology within a given cell, calculating the relative hardness of substrate and abrasive. Abrasion is switched off when clast hardness is lower than the substrate, whereas Melanson (2012) neglects the clast-substrate hardness differential. Hildes (2001) also uses lithology dependent quarrying rate factors, although the accuracy of this is questionable as quarrying primarily relies on the density of pre-existing joints and weaknesses in the substrate (Hooyer et al., 2012; Iverson, 2012). Joint and fracture density is not easily quantified at the relevant scales and is highly variable within the dimension of a grid cell (e.g. km to 100's km). Hildes et al. (2004) and Melanson (2012) both use estimates of cavitation (from basal water pressure) in the lee side of basal protrusions to estimate stress regimes and thus quarrying rates. Both models give englacial transport rates through advection, however, Hildes (2001) omits subglacial transport.

B1 Abrasion Law

Abrasion occurs from contact between two surfaces either through polishing or through striation (Benn and Evans, 2010). Polishing is the process by which the abrading surface removes protrusions in the bed reducing its roughness. Striation is the process by which stress caused by asperities in the abrading surface generate fracture sets which accumulate as linear troughs behind the asperity. Abrasion in the GSM is given by (Melanson et al., 2013):

$$\dot{A} = \exp\left(-h_{sed}/\tilde{h}_{sed}^*\right) \frac{k_{abr}}{HV^*} \sum_R C_b(R) F_N(R) |v_{par}(R)| \quad (B1)$$

The exponential represents a shielding coefficient – decreased contact between the abrading surface and the substrate as sediment accumulates. h_{sed} is the sediment layer thickness and \tilde{h}_{sed}^* is a characteristic thickness for shielding (shielding factor). This shielding factor is taken by Hildes (2001) to represent the areal fraction of the rough bed within a given cell which is covered by sediment. Hildes (2001) calculates this as

$$\tilde{h}_{sed}^* = \tilde{d}_1 \theta_{mean} + \tilde{d}_0 \quad (B2)$$

where $\tilde{d}_1 = 10.0\text{m}$ and $\tilde{d}_0 = 2.0\text{m}$ and bed dip $\theta_{mean} \in [0, 0.45]$ (deg) so that $\tilde{h}_{sed}^* \in [2.0, 6.5]$. Here, since this range of bed dips was defined using coarser resolution digital elevation maps (30-1000 m horizontal resolution, § 2.1 in Hildes, 2001), the assumed a priori range of \tilde{h}_{sed}^* is widened to $[2.0, 20.0]$ as higher resolution could pick up steeper (rougher) beds. The abrasion coefficient C_{abr}^* is a tuning parameter defined as

$$C_{abr}^* = k_{abr}/HV^*. \quad (B3)$$

The abrasion wear coefficient, k_{abr} , is shown in Hildes (2001) to vary over 2 orders of magnitude from $[0.002, 0.3]$ on the basis of reference to the literature. HV^* is the Vickers hardness. Since the substrate hardness does not appear here it is



560 implicitly assumed that the substrate is softer than the abrading material. From review of the literature, Hildes (2001) gives a range of Vickers hardness values of $HV^* \in [0.3 \times 10^{-9}, 12 \times 10^{-9}]$ Pa. This gives the range of abrasion coefficient: $C_{abr} \in [1.7 \times 10^5, 1.0 \times 10^9]$. Experiments by Iverson (1990) (granitic fragments frozen into ice and pressed into a sliding marble substrate) found that abrasion in their experiments more closely resembled the abrasion law of Hallet (1979) than that of Boulton (1979).

565 C_b is entrained debris concentration at a range of sediment radii (R), calculated from the englacial sediment concentration at the bottom (first) layer, C_{eng}^1 (see § ??) assuming volume concentration is equal to areal concentration:

$$C_b(R) = \frac{C_{eng}^1 \exp\left\{-\left(\log_{10}(R) - \log_{10}(E[R])\right)^2 / (2 \log_{10} \text{Var}[R])\right\}}{\pi R^2 \sum \exp\left\{-\left(\log_{10}(R) - \log_{10}(E[R])\right)^2 / (2 \log_{10} \text{Var}[R])\right\}} \quad (\text{B4})$$

F_N is the normal force between bed and abrading particle, v_{par} is the speed of the abrasive across the bed. These last two factors are calculated according to two different models of subglacial abrasion: the Boulton model assumes the normal force is proportional to the effective pressure N_{eff} while particle velocity is reduced by a particle size, effective pressure, and ice flow dependent drag terms.

$$F_N = A_e P_e \quad (\text{B5})$$

$$v_{par}(R) = |v_s| - 2B_g^* R \left(\frac{\mu^* P_e A_e}{A_r} \right)^3 - \frac{P_m P_e A_e}{2L_{fus} \rho_i A_r R} \quad (\text{B6})$$

575 Conversely, the Hallet model assumes the normal force is proportional to particle size and normal velocity (from normal component ice velocity due to subgrid bed undulation and basal melt rate). Hallet's particle velocity also assumes a slow down from bed contact, assuming equilibrium between friction with the bed and "drag" from the ice.

$$F_N(R) = f_{bed}^N \frac{4\pi\eta R^3}{\tilde{R}^2 + R^2} v_n \quad (\text{B7})$$

$$580 \quad v_{par} = |v_s| \left(1 - \frac{\mu^* f_{bed}^N \sin\theta}{f_{bed}^T} \right) - \frac{\mu^* f_{bed}^N}{f_{bed}^T} \dot{b}_{melt} \quad (\text{B8})$$

Abrasion is turned off when abrading particle velocity reaches zero, ice becomes cold-bedded, or N_{eff} reaches zero (flotation).

B2 Quarrying Law

585 Quarrying is also an erosive process like abrasion, but produces larger (> 1 cm) fragments of rock, taking advantage of joints (weaknesses in the rock Benn and Evans, 2010) as seen in the control of quarried surface orientation toward pre-existing joint and fracture sets over sliding direction (Hooyer et al., 2012). Stress gradients due to cavity growth concentrate force on bedrock



steps where these forces can exceed 50% higher than ambient ice-bed pressures (Iverson, 1991). Separation pressure, P_s , is given in Melanson et al. (2013); Cuffey and Paterson (2010) as:

$$P_s = P_{ice} - \frac{\tau_b}{\pi \zeta^*} \quad (\text{B9})$$

590 where P_{ice} is ice overburden, τ_b is basal shear stress (assumed to be driving stress), and ζ^* is basal roughness (protrusion height over distance between).

ζ^* is similar to the basal roughness h_r in the linked-cavity hydrology formulation. Additionally, Melanson (2012) assumes the grid-scale cavity extent (important for quarrying rate) is proportional to the residual pressure (difference between water pressure and separation pressure). However cavity extent is given in linked-cavity hydrology directly by the grid-scale subglacial water thickness h_{wb} . Because of this dependence on cavity formation, where quarrying rates are large, linked-cavity drainage may be dominant.

The quarrying rate in Melanson et al. (2013) is given by:

$$\dot{Q} = \exp\left(-h_{sed}/\tilde{h}_{sed}^*\right) C_{quar}^* \left(\frac{P_w - P_s}{\tilde{P}_r}\right)^{n_p^*} \quad (\text{B10})$$

with C_{quar}^* the quarrying coefficient, n_p^* an exponent controlling residual pressure contribution, \tilde{P}_r the characteristic residual pressure ($\approx 18kPa$)

B3 Empirical Erosion Law

The empirical erosion rate used in the GSM is (Melanson et al., 2013)

$$\dot{E}_{emp} = \exp\left(-h_{sed}/\tilde{h}_{sed}^*\right) C_{emp}^* |\tau_b| |v_s| \quad (\text{B11})$$

with C_{emp}^* a coefficient and v_s the sliding velocity.

605 B4 Englacial Transport: Entrainment, Mixing, and Advection

Englacial transport in the GSM is (Melanson et al., 2013)

$$\frac{\partial C}{\partial t} = -\nabla \cdot C \mathbf{v}_i - \frac{\partial(C \dot{V}_{net})}{\partial z} + V_{mix} \quad (\text{B12})$$

The lateral velocities v_i are a function of lateral and vertical position. The entrainment/deposition rate V_{net} is a function of lateral position. The vertical mixing rate V_{mix} is diffusion of sediment concentration between layers which varies laterally and vertically. Within the GSM, vertical diffusion and lateral advection are treated separately with lateral advection calculated first for a given time step. A tri-diagonal matrix solver is used to calculate the sediment concentrations due to vertical diffusion. Vertical mixing is given by:

$$V_{mix} = \frac{\partial}{\partial z} \left(D \frac{\partial C}{\partial z} \right) \quad (\text{B13})$$



$$615 \quad D = \tilde{D}^* \left(\frac{|v_s|}{\tilde{v}_s} \right) e^{-z/\tilde{z}^*} e^{-h_{sed}/\tilde{h}^*} \quad (\text{B14})$$

Where \tilde{D}^* , \tilde{z}^* , and \tilde{h}^* are scale factor parameters and \tilde{v}_s is a scale factor based on typical sliding velocities. Vertical diffusion decreases with increased sediment cover because where there is more soft sediment there will be less folding within the basal ice and thus less vertical (eddy) diffusion. This is because basal stress is balanced by viscous or plastic forces within the soft-deformation layer instead of by the process of folding in basal ice.

620 Sediment is entrained within the ice by regelation (Iverson and Semmens, 1995). The rate of regelation of ice into the sediment is given by:

$$v_r = K_s \frac{N_{eff}}{l_a} \quad (\text{B15})$$

where K_s is the conductivity of ice into the sediment layer (defined in Hildes (2001, eqn. 4.4 and 4.5)) and l_a is the englacial sediment array thickness. This array thickness acts to limit sediment entrainment as the medium transitions from ice supported
 625 to clast supported and the medium can no longer regelate around sediment grains. The effective array depth is the series of smoothed step functions of sediment thickness within each basal grid layer:

$$l_a = \sum_{k_z} l_{mod}(k_z) \Delta z(k_z) \quad (\text{B16})$$

$$l_{mod}(z) = 0.5 \{ \tanh [20 (C(z) - C_{crit}^*)] + 1 \} \quad (\text{B17})$$

630 V_{net} term calculated as the net of entrainment (due to regelation) and deposition (due to basal melt), giving:

$$V_{net} = v_r - \frac{\dot{b}_{melt} C(z=0)}{1 - \phi^*} \quad (\text{B18})$$

where the sediment concentration in the bottom layer is deposited with porosity ϕ^* when melting (\dot{b}_{melt}) occurs. This implies recently entrained sediment has concentration $C(z=0) = 1 - \phi^*$. Entrainment rate is capped at value v_{max}^* and layer concentration is capped at C_{max}^* .

635 Discretization above the ice-sediment interface used for modelling entrainment, mixing, and advection of sediment in the ice uses an exponential grid. This exponential grid concentrates resolution in the most dynamic basal layers where mixing/entrainment velocities are highest. The ice-sediment interface moves up as sediment is deposited and down as bedrock is eroded or denuded. The grid is chosen uniform in ξ and transformed using:

$$z_{ice} = \frac{z_{max}}{\sum [e^{\xi/z_0}]} e^{\xi/z_0} \quad (\text{B19})$$

640 where $z_0 = 15$ is the exponential grid spacing parameter and $z_{max} = 23$ is the full height of the entrainment grid in the ice. This grid is depicted in fig. B1.

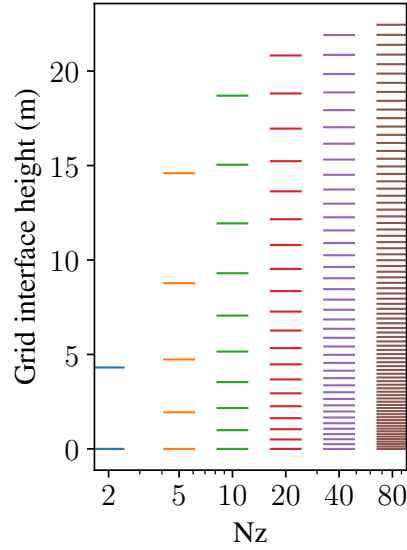


Figure B1. Depiction of the vertical englacial sediment grid for various resolutions.

B5 Subglacial Transport Law

Basal sediment transport is governed by the sediment continuity relationship given in Melanson et al. (2013):

$$\frac{\partial h_{sed}}{\partial t} = -\nabla \cdot \mathbf{Q}_s + \dot{E} - V_{net} \quad (\text{B20})$$

645 where sediment thickness through time is given as the sum of the convergence of subglacial transport through deformation, erosion rate \dot{E} (empirical or process), and entrainment rate. This acts with englacial transport in eqn. B12 to give the total sediment transport and production.

Subglacial transport from soft sediment deformation occurs as basal shear stress from the overbearing ice sheet is applied to a layer of unconsolidated till assumed to behave as a Coulomb plastic in the manner of Iverson (1985). The constitutive
 650 relationship presented therein is between the deformation rate tensor (\mathbf{D}) and the stress deviator tensor (\mathbf{T}):

$$\mathbf{D} = \begin{bmatrix} \frac{\partial v_x}{\partial x} & \frac{1}{2} \left(\frac{\partial v_x}{\partial y} + \frac{\partial v_y}{\partial x} \right) & \frac{1}{2} \left(\frac{\partial v_x}{\partial z} + \frac{\partial v_z}{\partial x} \right) \\ \frac{1}{2} \left(\frac{\partial v_y}{\partial x} + \frac{\partial v_x}{\partial y} \right) & \frac{\partial v_y}{\partial y} & \frac{1}{2} \left(\frac{\partial v_y}{\partial z} + \frac{\partial v_z}{\partial y} \right) \\ \frac{1}{2} \left(\frac{\partial v_z}{\partial x} + \frac{\partial v_x}{\partial z} \right) & \frac{1}{2} \left(\frac{\partial v_z}{\partial y} + \frac{\partial v_y}{\partial z} \right) & \frac{\partial v_z}{\partial z} \end{bmatrix} \quad (\text{B21a})$$

$$\mathbf{T} = \begin{bmatrix} \tau_{xx} + p & \tau_{xy} & \tau_{xz} \\ \tau_{yx} & \tau_{yy} + p & \tau_{yz} \\ \tau_{zx} & \tau_{zy} & \tau_{zz} + p \end{bmatrix} \quad (\text{B21b})$$



where v_i is the i^{th} component of velocity, τ_{ij} are the components of deviator stress, and $p = -\frac{1}{3}(\tau_{xx} + \tau_{yy} + \tau_{zz})$. Iverson
655 (1985) then uses a generalization of the Coulomb criterion for plastic yield, the extended Von Mises (Von Mises, 1913) criterion
— Drucker and Prager (1952, eqn. 2):

$$II_T^{1/2} = k + \alpha p \quad (\text{B22})$$

where II_T is the second invariant of the stress deviator tensor, k is the cohesion and α is the tangent of the angle of internal
friction. This is

$$660 \quad II_T = \frac{1}{2} [\text{tr} T^2 - \text{tr} T^2] \quad (\text{B23})$$

$$= \frac{1}{2} [(\tau_{xx} + p)^2 + (\tau_{yy} + p)^2 + (\tau_{zz} + p)^2 + 2(\tau_{xy}^2 + \tau_{yz}^2 + \tau_{zx}^2)]. \quad (\text{B24})$$

Iverson (1985) then works out his constitutive equation:

$$\mathbf{T} = 2\mu\mathbf{D} + \frac{k + \alpha p}{II_D^{1/2}}\mathbf{D} \quad (\text{B25})$$

where

$$665 \quad II_D^{1/2} = \begin{cases} \frac{1}{2\mu} [II_T^{1/2} - (k + \alpha p)] & II_T^{1/2} > k + \alpha p \\ 0 & II_T^{1/2} \leq k + \alpha p \end{cases}. \quad (\text{B26})$$

In the context of the shallow ice approximation (no lateral or longitudinal shear components) and assuming no vertical transport
(vertical length scales are much shorter than lateral when comparing the horizontal dimensions of ice sheets against vertical
dimensions of till beds), the deformation and stress tensors become:

$$\mathbf{D} = \begin{bmatrix} 0 & 0 & \frac{1}{2} \left(\frac{\partial v_x}{\partial z} + \right) \\ 0 & 0 & \frac{1}{2} \left(\frac{\partial v_y}{\partial z} \right) \\ \frac{1}{2} \left(\frac{\partial v_x}{\partial z} \right) & \frac{1}{2} \left(\frac{\partial v_y}{\partial z} \right) & 0 \end{bmatrix} \quad (\text{B27a})$$

670

$$\mathbf{T} = \begin{bmatrix} 0 & 0 & \tau_{xz} \\ 0 & 0 & \tau_{yz} \\ \tau_{zx} & \tau_{zy} & 0 \end{bmatrix} \quad (\text{B27b})$$

, this also assumes incompressible shear such that $\tau_{xx} = \tau_{yy} = \tau_{zz} = -p$. This p is the effective pressure with sediment over-
burden, $N_{eff} + \Delta\rho g z$. Using a similar model of subglacial deformation, Pollard and Deconto (2009) assumes $N_{eff} = 0$ so
that the normal stress is only applied by the sediment overburden. The model in the GSM follows Jenson et al. (1995) and take
675 the normal stress as $N_{eff} + (\rho_s - \rho_w)gz$ with z the depth into sediment. Jenson et al. (1995) then shows that the independent
lateral components are:

$$\tau_{xz} = (2D_0)^{(n_s-1)/n_s} \mu_0 \left(\frac{dv_x}{dz} \right)^{1/n_s} + c + (N_{eff} + \Delta\rho g z) \tan \phi^* \quad (\text{B28a})$$



$$\tau_{yz} = (2D_0)^{(n_s-1)/n_s} \mu_0 \left(\frac{dv_y}{dz} \right)^{1/n_s} + c + (N_{eff} + \Delta\rho gz) \tan \phi^* \quad (\text{B28b})$$

680 τ_{xz} and τ_{yz} are the x/y components of ice basal shear stress. Rearranging for v_i (i^{th} component of sediment velocity) gives:

$$v_i = \int \left[\frac{\tau_{iz} - c - (N_{eff} + \Delta\rho gz) \tan \phi^*}{(2D_0)^{\frac{n_s-1}{n_s}} \mu_0} \right]^{n_s} dz \quad (\text{B29})$$

$$= \frac{[\tau_{iz} - (c + N_{eff} \tan \phi^* + \Delta\rho gz \tan \phi^*)]^{n_s+1} / (n_s + 1)}{\left[(2D_0)^{\frac{n_s-1}{n_s}} \mu_0 \right]^{n_s} \Delta\rho g \tan \phi^*} + \gamma_1 \quad (\text{B30})$$

Where γ_1 is the constant of integration. Assuming a reference frame of zero background flow of sediment, this constant is $\gamma_1 = 0$. At the ice-sediment interface, $z = 0$,

$$685 \quad v_i = \frac{[\tau_{iz} - c - N_{eff} \tan \phi^*]^{n_s+1}}{(n_s + 1) (2D_0)^{n_s-1} \mu_0^{n_s} \Delta\rho g \tan \phi^*} \quad (\text{B31})$$

Deformation thickness is found by solving for $v_i(z = z_d) = 0$:

$$0 = \tau_{iz} - c - N_{eff} \tan \phi^* - \Delta\rho gz_d \tan \phi^* \quad (\text{B32})$$

$$\Rightarrow z_d = \frac{\tau_{iz} - c - N_{eff} \tan \phi^*}{\Delta\rho g \tan \phi^*} \quad (\text{B33})$$

Integrating once more to get flux over the deformation thickness,

$$690 \quad Q_i = \int_{z_d}^0 v_i dz = - \int_{z_d}^0 \frac{[\tau_{iz} - c - N_{eff} \tan \phi^* - \Delta\rho gz \tan \phi^*]^{n_s+1}}{\left[(2D_0)^{\frac{n_s-1}{n_s}} \mu_0 \right]^{n_s} \Delta\rho g \tan \phi^* (n_s + 1)} dz \quad (\text{B34})$$

$$= \frac{(\Delta\rho g \tan \phi^*)^{n_s} (n_s+1)}{\left[(2D_0)^{\frac{n_s-1}{n_s}} \mu_0 \right]^{n_s} (\Delta\rho g \tan \phi^*)^2 (n_s + 1) (n_s + 2)} \quad (\text{B35})$$

$$Q_{sx} = \begin{cases} 0 & \text{ice floating} || \text{freezing} || H \leq 0. \end{cases}$$

$$Q_s = \begin{cases} h_{sed} \leq z_p & \frac{\left[-\frac{(\tau - c_{cohe} - N_{eff} + (\rho_s - \rho_w)g \tan \phi h_{sed})^{n_s+2}}{(n_s+2)(\rho_s - \rho_w)g \tan \phi} - (\tau - c_{cohe} - N_{eff} \tan \phi)^{n_s+2} - [\tau - c_{cohe} - (N_{eff} + (\rho_s - \rho_w)g h_{sed}) \tan \phi]^{n_s+1} h_{sed} \right]}{(n_s+1)(2D_0)^{n_s-1} \mu_0^{n_s} (\rho_s - \rho_w)g \tan \phi} \\ h_{sed} > z_p & \frac{-1}{(n_s+1)(n_s+2)(2D_0)^{n_s-1} \mu_0^{n_s} [(\rho_s - \rho_w)g \tan \phi]^2} [(-\tau - c_{cohe} - N_{eff} \tan \phi)^{n_s+2}] \end{cases}$$

695 Appendix C: Model Verification

We verify the model in three ways: symmetry of solutions, convergence under increasing resolution, and mass conservation. All model solutions were found to be symmetric. The temporal convergence tests are in § C1, spatial in § C2, number of bed dips in the abrasion calculation in § C3, number of grain sizes in the abrasion calculation in § C4, and number of vertical levels in the englacial transport grid in § C5. Mass conservation test is in § C6.

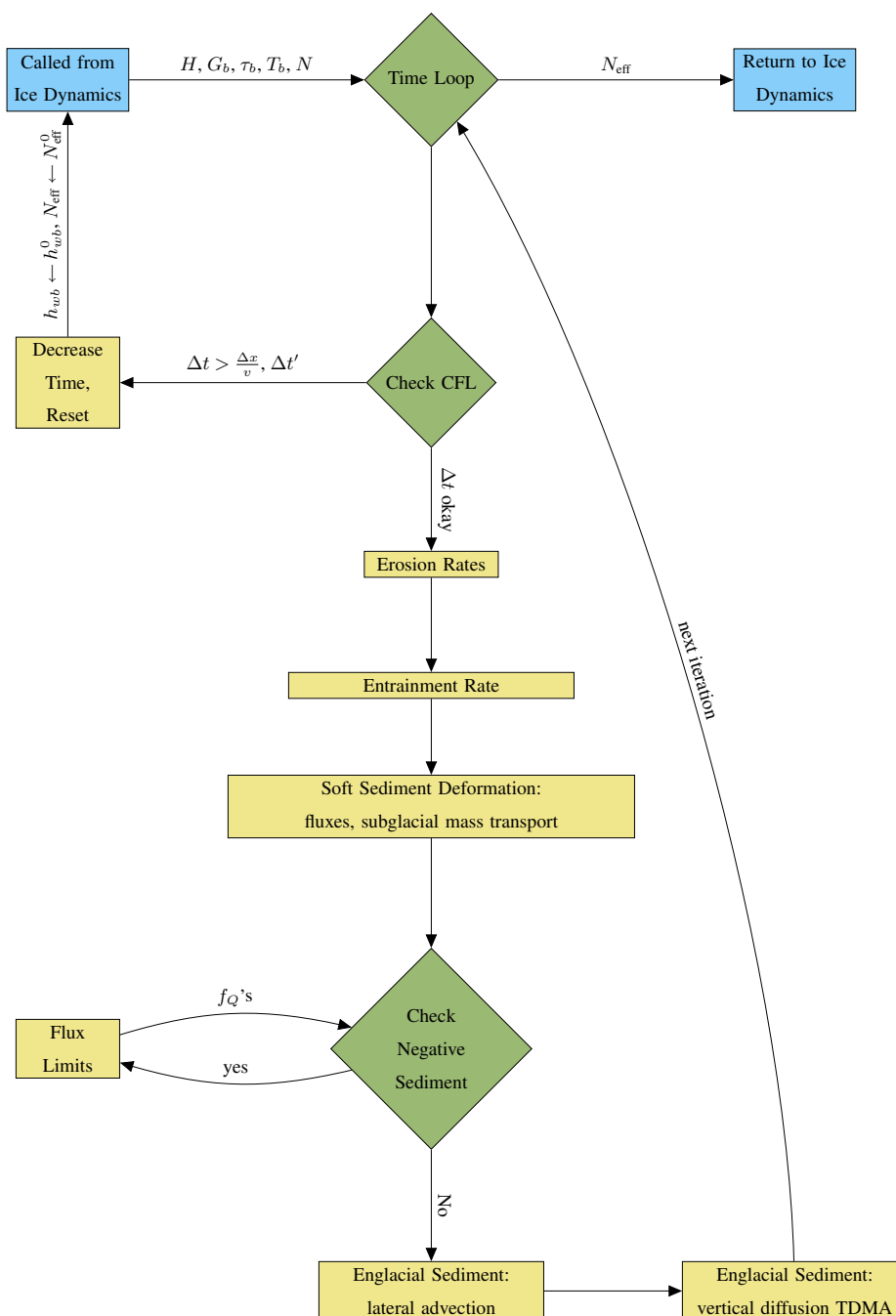


Figure B2. Flow chart of sediment model algorithm execution

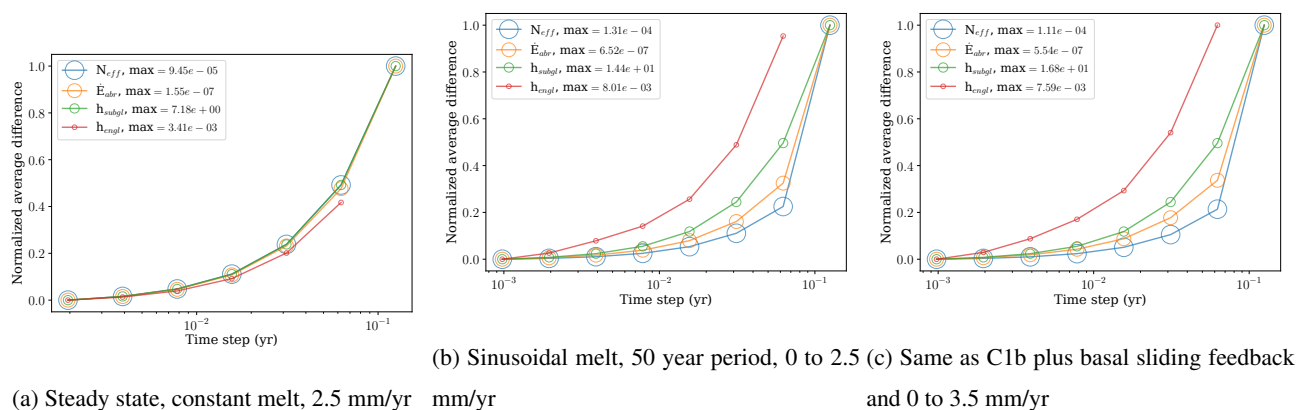


Figure C1. Convergence with decreasing time step. Each metric is normalized such that the scale is consistent across metrics. The normalization factor shown in the legend (max).

C1 Temporal convergence test

700 As a test of convergence under increasing temporal resolution (decreasing time step length) the sediment model was run to steady state under SHMIP scenario A (constant 2.5 mm/a de Fleurian et al., 2018), a sinusoidal melt forcing with constant sliding velocity, and sinusoidal melt forcing with coupled basal velocity. The convergence is shown in fig. C1. Under this scenario quarrying never switched on owing to the low driving stress of the setup, but the quarrying rate is numerically similar to (and simpler than) abrasion. Convergence is shown for the effective pressure N_{eff} , abrasion rate \dot{E}_{abr} , subglacial sediment thickness h_{subgl} , and englacial sediment thickness h_{engl} . The effective pressure solution converged most quickly followed by abrasion rate, and lastly the subglacial and englacial convergence were about the same (englacial not captured for highest time step).

705 C2 Spatial convergence test

Here we show the effect of varying spatial resolution on the model solution. The models are run to steady state with prescribed melt and basal velocity (1.75 m/a ice and 2.0 m/a respectively) in the SHMIP setup (de Fleurian et al., 2018). The square root ice sheet flowline length from divide to toe is 100 km and the number of cells varied between 2,45. The model solution at each resolution is linearly interpolated to the highest resolution grid and the absolute sum of the difference against the highest resolution solution is used for the error.

710 Fig. C2 shows the convergence of model solutions (same set as fig. C1) at increasing spatial resolution (shorter cell width).

C3 Number of bed dips convergence test

Here we show convergence under an increasing number of bed dips relevant for calculating normal force and velocities in the abrasion rate calculation. The abrasion rate model solution converges with an increasing number of dips. To optimize model performance, the number of bed dips was chosen at $NUMBEDDIP = 10$ (see fig. C3). Resolutions tested are $\{5i\}$ for $i \in [1, 18]$, $i \in \mathbb{N}$ for uniform distribution of angles, $\theta_{dip} \in [-34^\circ, +34^\circ]$.

715 C4 Number of grains size bins convergence test

The grain size distribution is used to calculate normal force and particle velocity in the abrasion rate. The abrasion rate solution converges with an increasing number of bins in the grains size distribution (fig. C4). Between 5 and 360 bins were tested and showed small error between the lowest and highest number of bins. As such 10 bins was chosen to optimize model performance.

C5 Englacial grid resolution test

720 The englacial grid is used in the vertical diffusion of sediment during englacial transport. A depiction of the non-linear grid is shown in fig. C5. The number of englacial grid levels was tested between 2 and 80, with 10 chosen to optimize model performance (10 bins had $< 10\%$ error relative to highest bin count, see fig. C5).

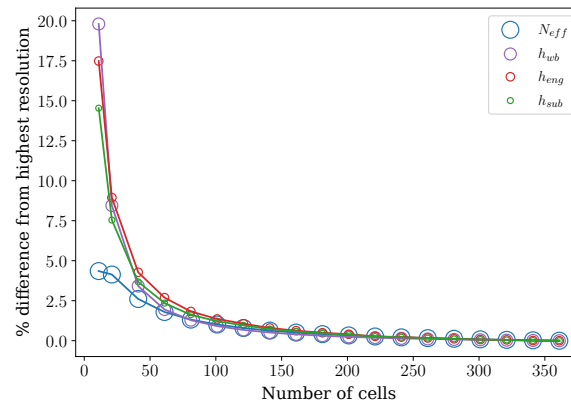


Figure C2. Difference in mean flowline solutions for unsteady SHMIP square root ice sheet topography as a function of increasing spatial resolution, at the end of 10 kyr run.

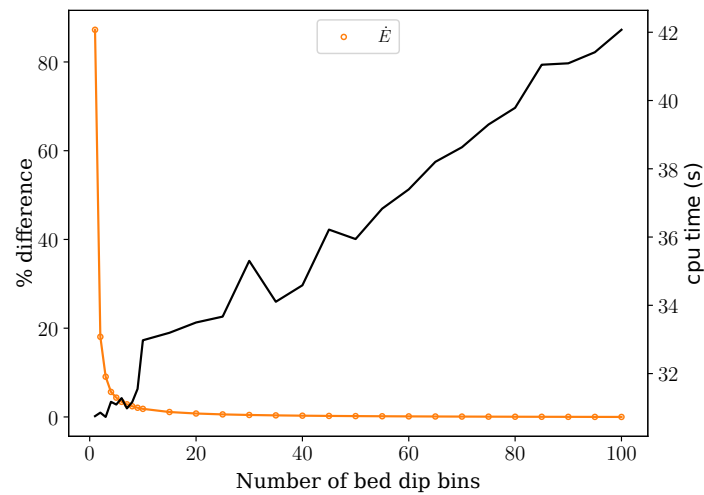


Figure C3. L2 norm between each resolution and the highest resolution run, normalized by highest resolution run.

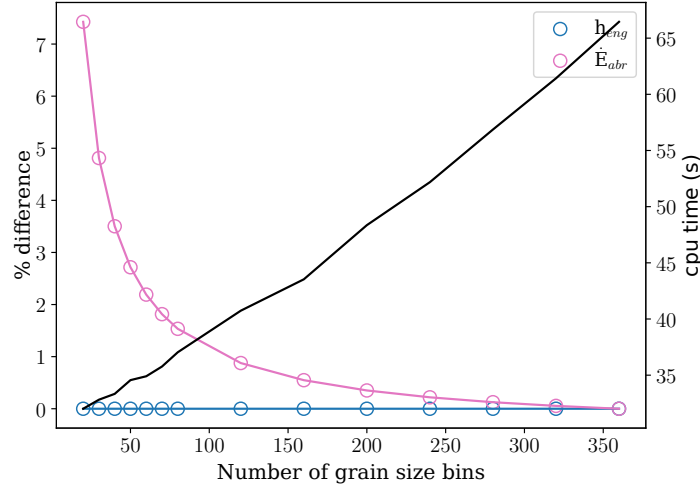


Figure C4. L2 norm between each resolution and the highest resolution run, normalized by highest resolution run.

C6 Mass conservation test

725 The integral of the total erosion and removal of sediment over the ice sheet extent less the subglacial and englacial fluxes at the margin will give the total sediment within the ice sheet extent (subglacial and englacial). To test mass balance with unsteady input, we applied a sinusoidal meltwater forcing (eqn. ??) to the *SQRT_TOPO* setup with a basal sliding velocity coupled to effective pressure. The sediment mass balance is calculated as the balance of inputs and outputs:

$$net_{sed}^{t_i} = \int_0^{t_i} \left(\int_A \dot{E}_{abr} + \dot{E}_{quar} da - \oint_S \left[\mathbf{Q}_{subgl} + \mathbf{U}_b \int_0^{z_{engmax}} C_{eng} dz \right] \cdot \mathbf{n} dS \right) dt - h_{subgt}^{initial} \quad (C1)$$

$$ERR_{sed}^{t_i} = \frac{|net_{sed}^{t_i} - V_{sed}^{t_i}|}{V_{sed}^{t_i}} \quad (C2)$$

where $V_{sed}^{t_i}$ is the total subglacial and englacial sediment within the ice sheet extent at time step t_i .

730 Appendix D: Sediment Loading and Isostatic Adjustment Test

We initialize the bed with the present day isostatic equilibrium, impose the sediment load (increasing from experiment to experiment) and run to near equilibrium over 40 kyr. For these tests the CO_2 was set to 700 ppm to suppress ice growth (no ice developed), this melted ice over Ellesmere and the stub Greenlandic ice sheet. The change in topographic elevation (less sediment thickness) is plotted in fig. D1 and shows increased subsidence with increasing sediment load.

Appendix E: Produced and pre-existing sediment

735 Appendix F: Bed Dip Distribution for Abrasion Calculation

In the case of the Hallet abrasion model, the weathering rate is dependent on the angle of ice flow with respect to the bed. In order to account for the subgrid distribution of bed dip angle, we use the 2m lateral resolution ArcticDEM digital surface model (DSM) (Porter et al., 2023).

A given point and those above and to the left of that point all lie within a plane and give two vectors lying within that plane.

$$P1P0 = P1 - P0 \quad (F1)$$

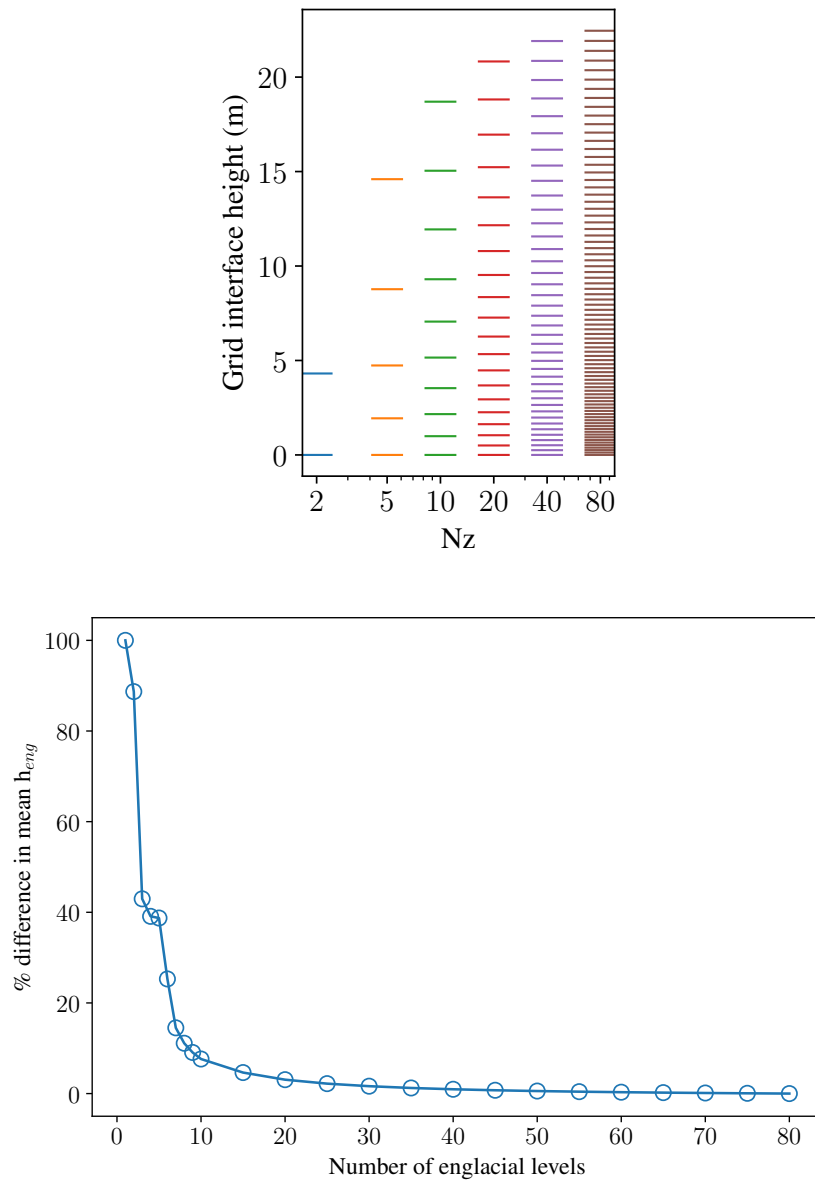


Figure C5. Convergence of englacial sediment thickness with more levels in the exponential englacial sediment grid.

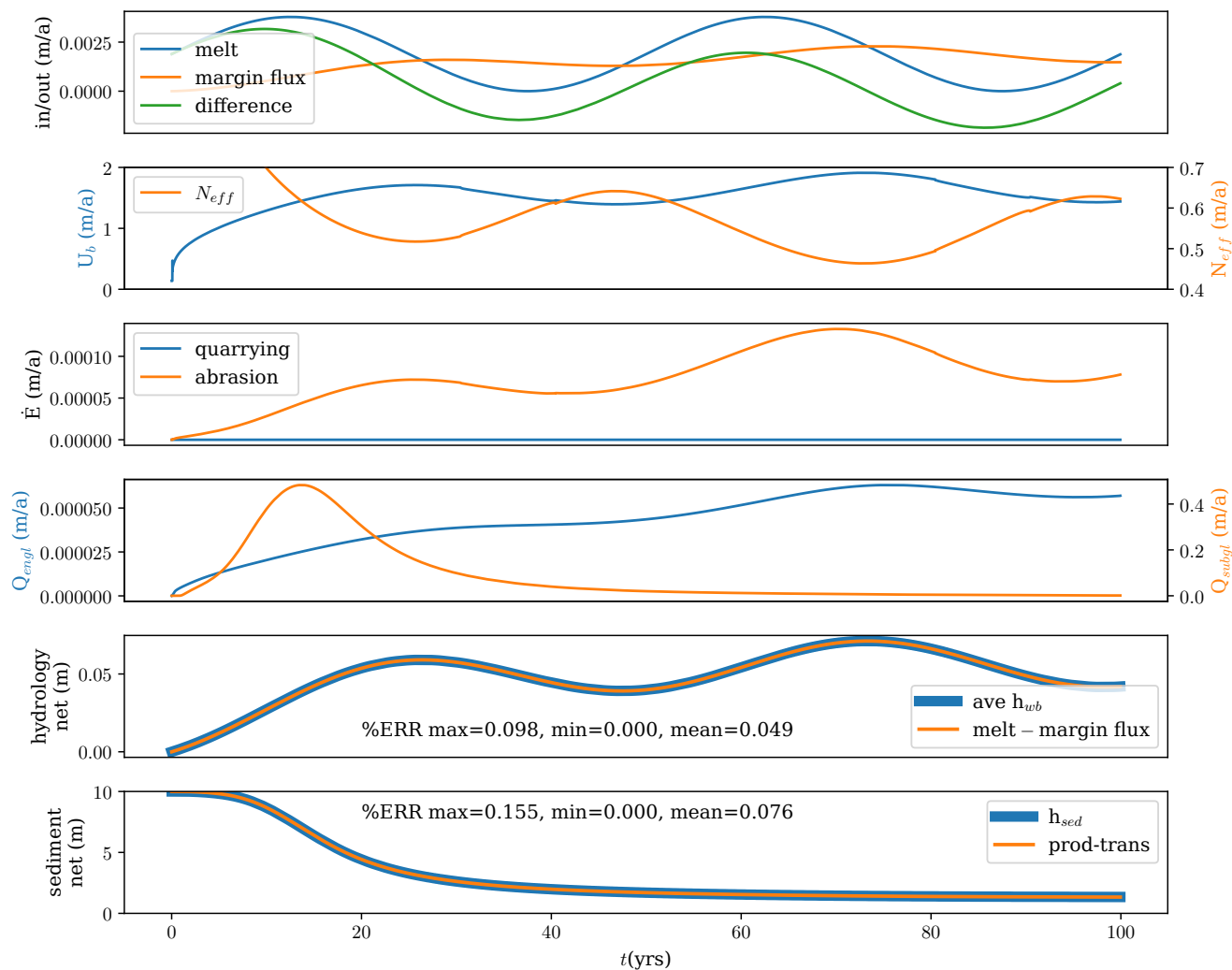


Figure C6. Mass conservation for sinusoidal melt input Mass balance for subglacial hydrology and basal sediment models given square root ice sheet topography and sinusoidal ice sheet basal mass balance (ice thickness, m/a), $Gb = 3.5 \times 10^{-3}/2 \sin 2\pi t/1000 + 3.5 \times 10^{-3}/2$. Basal sliding velocity calculated from driving stress and effective pressure.

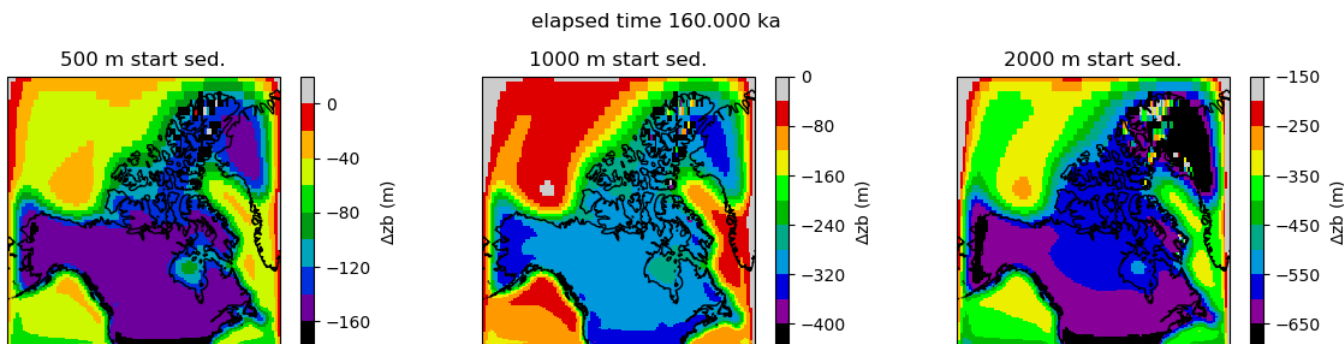


Figure D1. These isostatic adjustment tests show 40 kyr of isostatic adjustment (topographic effect of the sediment itself is removed) following sediment load emplacement. The load is imposed uniformly over the whole model domain: 500, 1000, and 2000 m.

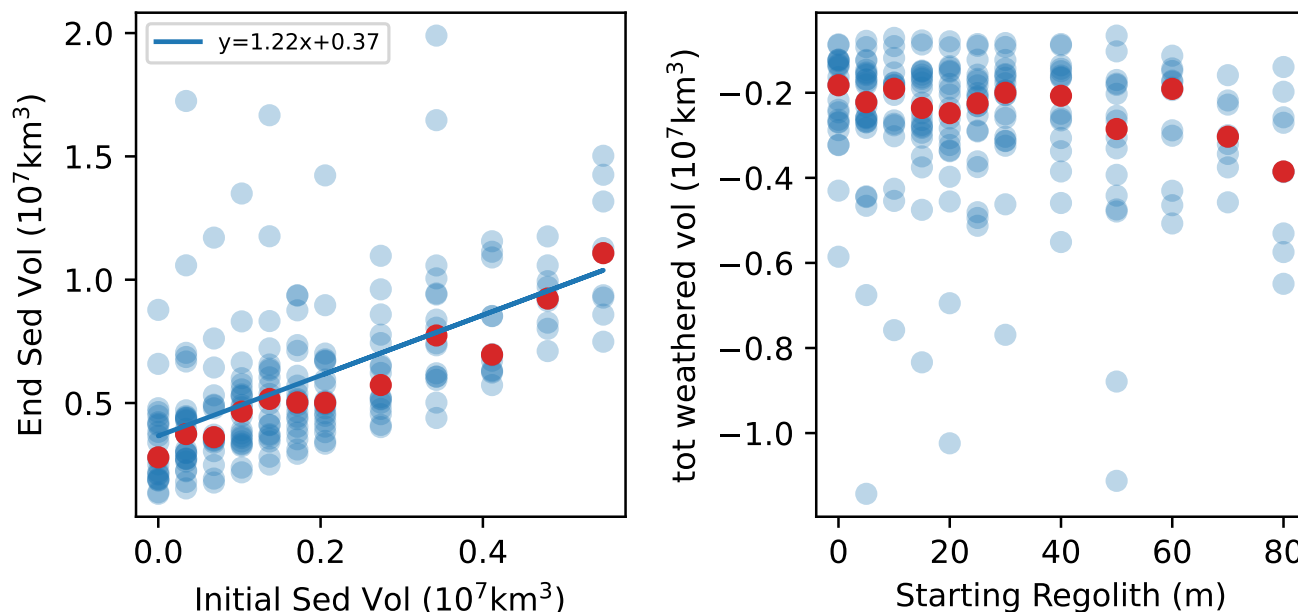


Figure E1. A comparison of the amount of sediment produced during glaciation with the amount of pre-existing regolith. The lefthand panel shows final sediment volume against initial sediment volume with a nearly one to one (1.22) linear slope – the final sediment volume is controlled mostly by input (initial) sediment volume. The righthand panel shows the total weathered (produced) volume of sediment against initial regolith thickness. The bulk volume of sediment produced is largely independent of the starting thickness. Around one to four million km^3 of sediment is produced throughout the Pleistocene – on the same order as the y-intercept in the lefthand plot.

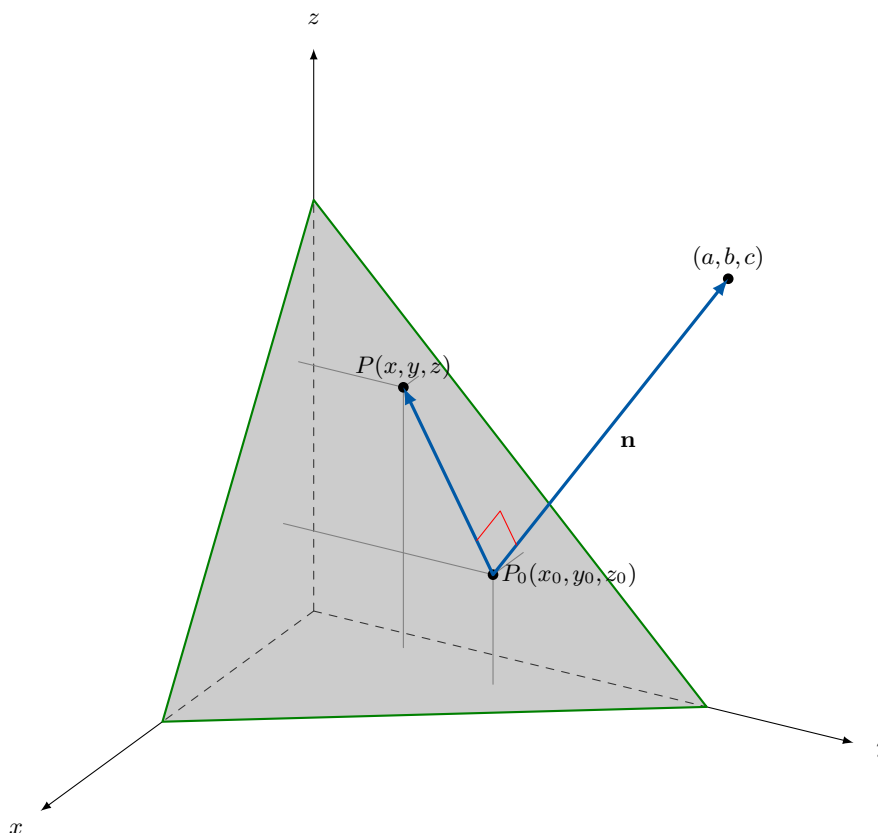


Figure F1. Illustration of calculating the normal vector to a plane from two non-colinear vectors lying within that plane.

740

$$P_2P_0 = P_2 - P_0 \tag{F2}$$

The normal vector to that plane can be expressed as the cross product of these two vectors,

$$P_{norm} = P_1P_0 \times P_2P_0 \tag{F3}$$

The dip angle between the approximated plane and the surface of the geoid is then

$$745 \quad \theta_{dip} = \arccos \frac{P_{norm} \cdot n_{geoid}}{\|P_{norm}\| \|n_{geoid}\|} \tag{F4}$$

In the NSIDC Sea Ice Polar Stereographic North projection the geoid normal unit vector has a z-component only. The dip angle then becomes:

$$\theta_{dip} = \arccos \left[\frac{P_{norm}}{\|P_{norm}\|} \right]_z \tag{F5}$$

Here we calculate these dip angles for both the covered and exposed bedrock regions of ArcticDEM coverage within onshore Canadian territory (shown in fig. F2). The two distributions are compared in fig. F3. We find negligible difference in distribution between these two domains with maximum likelihood dip angle around 0.55° and truncate the distribution at 10° . This hard bed dip angle distribution is used to calculate the abrasion rates throughout this paper.

750

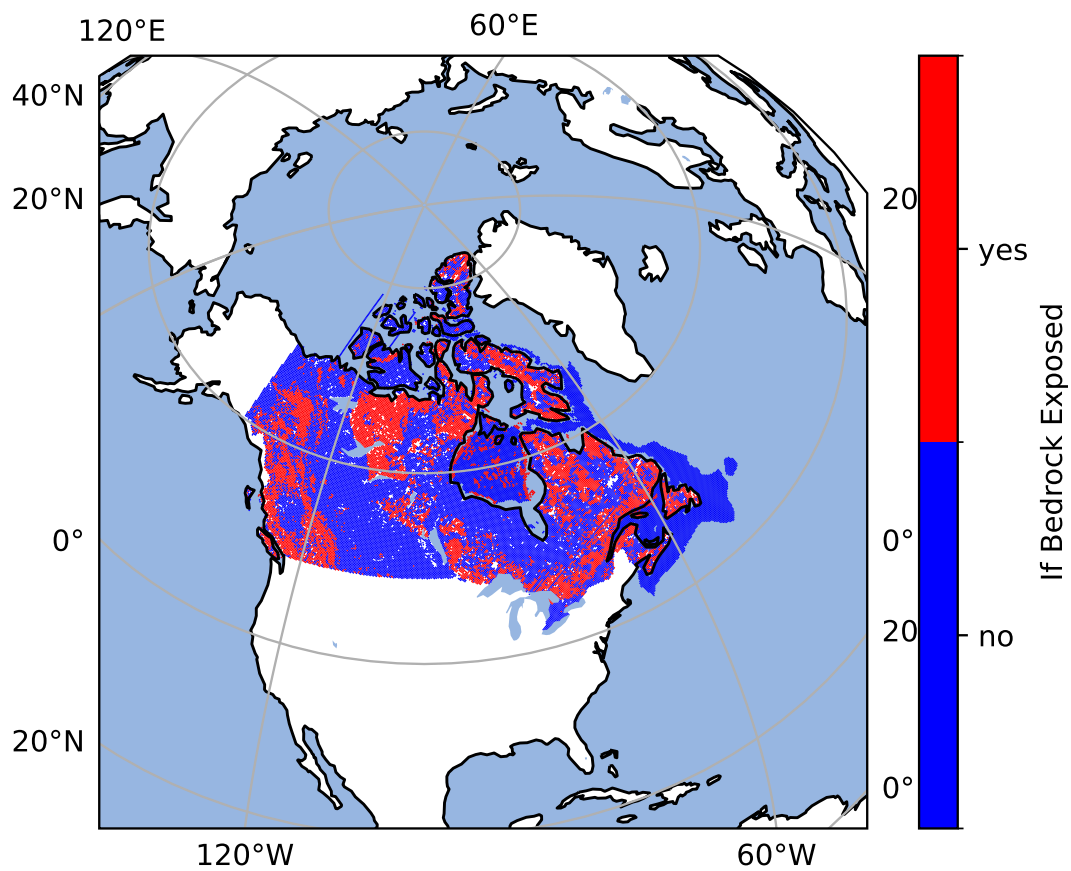


Figure F2. Map of exposed (hard, red) and covered (soft, blue) bedrock regions across Canada. Hard regions are those determined as either undifferentiated bedrock or till veneer in Fulton (1995), everything else is deemed soft (equivalently covered bedrock).

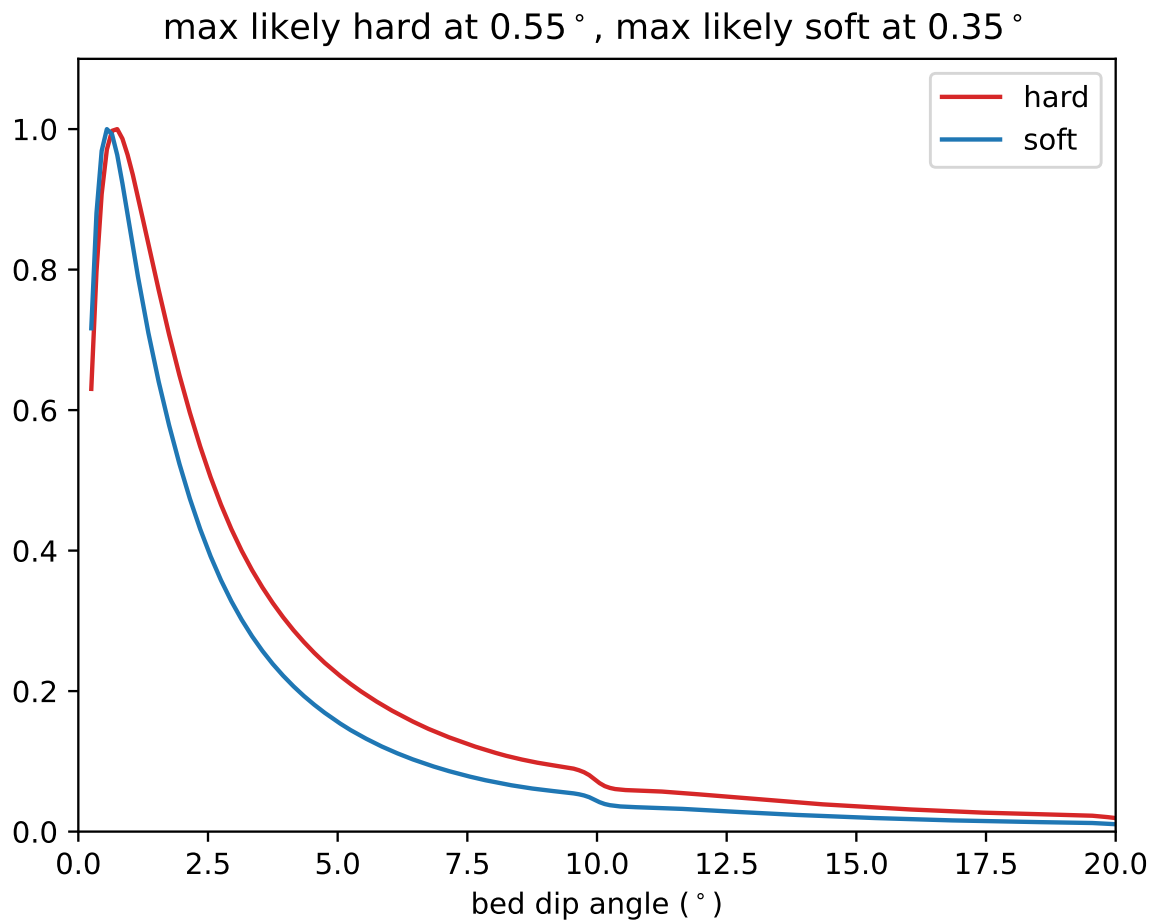


Figure F3. Dip angle distribution for hard and soft bedded regions shown in fig. F2.

Author contributions. MD performed sediment model development, devised/implemented the hydrology/sediment/ice dynamics coupling, experimental design & execution, analysis, and writing. LT maintains the GSM, devised/implemented the sediment/GIA coupling, advised experimental design, and edited the manuscript.

Competing interests. The authors declare no competing interests

755 *Acknowledgements.* We thank Stewart Jamieson for helpful discussion and review of an earlier version of this manuscript in his role as external Thesis examiner for MD.



References

- Surficial geology of Canada, <https://doi.org/10.4095/295462>, 2014.
- 760 Abril-Pla, O., Andreani, V., Carroll, C., Dong, L., Fannesbeck, C. J., Kochurov, M., Kumar, R., Lao, J., Luhmann, C. C., Martin, O. A.,
Osthege, M., Vieira, R., Wiecki, T., and Zinkov, R.: PyMC: a modern, and comprehensive probabilistic programming framework in
Python, *PeerJ Computer Science*, 9, e1516, <https://doi.org/10.7717/peerj-cs.1516>, 2023.
- Ahn, S., Khider, D., Lisiecki, L. E., and Lawrence, C. E.: A probabilistic Pliocene–Pleistocene stack of benthic $\delta^{18}\text{O}$ using a profile hidden
Markov model, *Dynamics and Statistics of the Climate System*, 2, <https://doi.org/10.1093/climsys/dzx002>, 2017.
- Alley, R. and Agustsdottir, A.: The 8k event: cause and consequences of a major Holocene abrupt climate change, *Quaternary Science*
765 *Reviews*, 24, 1123–1149, <https://doi.org/10.1016/j.quascirev.2004.12.004>, 2005.
- Alley, R. B. and MacAyeal, D. R.: Ice-rafted debris associated with binge/purge oscillations of the Laurentide Ice Sheet, *Paleoceanography*,
9, 503–511, <https://doi.org/10.1029/94pa01008>, 1994.
- Atkinson, L., Pawley, S., Andriashek, L., Hartman, G., Utting, D., and Atkinson, N.: Alberta Geological Survey Map 611 Sediment Thickness
of Alberta, Version 2, http://www.ags.gov.ab.ca/publications/MAP/PDF/MAP_611.pdf, 2020.
- 770 Austermann, J., Mitrovica, J. X., Latychev, K., and Milne, G. A.: Barbados-based estimate of ice volume at Last Glacial Maximum affected
by subducted plate, *Nature Geoscience*, 6, 553–557, <https://doi.org/10.1038/ngeo1859>, 2013.
- Balco, G. and Rovey, C. W.: Absolute chronology for major Pleistocene advances of the Laurentide Ice Sheet, *Geology*, 38, 795–798,
<https://doi.org/10.1130/g30946.1>, 2010.
- Bell, M. and Laine, E. P.: Erosion of the Laurentide Region of North America by Glacial and Glaciofluvial Processes, *Quaternary Research*,
775 23, 154–174, [https://doi.org/10.1016/0033-5894\(85\)90026-2](https://doi.org/10.1016/0033-5894(85)90026-2), 1985.
- Benn, D. I. and Evans, D. J. A.: *Glaciers & Glaciation*, Hodder Education, An Hachette UK Company, 338 Euston Road, London NW1 3BH,
2 edn., 2010.
- Bereiter, B., Eggleston, S., Schmitt, J., Nehrass-Ahles, C., Stocker, T. F., Fischer, H., Kipfstuhl, S., and Chappellaz, J.: Revi-
sion of the EPICA Dome C CO₂ record from 800 to 600 kyr before present, *Geophysical Research Letters*, 42, 542–549,
780 <https://doi.org/10.1002/2014gl061957>, 2015.
- Boulton, G.: Processes of Glacier Erosion on Different Substrata, *Journal of Glaciology*, 23, 15–38,
<https://doi.org/10.3189/s0022143000029713>, 1979.
- Braun, J., Zwartz, D., and Tomkin, J. H.: A new surface-processes model combining glacial and fluvial erosion, *Annals of Glaciology*, 28,
282–290, <https://doi.org/10.3189/172756499781821797>, 1999.
- 785 Brigham-Grette, J., Melles, M., Minyuk, P., Andreev, A., Tarasov, P., DeConto, R., Koenig, S., Nowaczyk, N., Wennrich, V., Rosen, P., and
et al.: Pliocene Warmth, Polar Amplification, and Stepped Pleistocene Cooling Recorded in NE Arctic Russia, *Science*, 340, 1421–1427,
<https://doi.org/10.1126/science.1233137>, 2013.
- Byerlee, J.: Friction of rocks, *Pure and Applied Geophysics PAGEOPH*, 116, 615–626, <https://doi.org/10.1007/bf00876528>, 1978.
- Chalk, T. B., Hain, M. P., Foster, G. L., Rohling, E. J., Sexton, P. F., Badger, M. P. S., Cherry, S. G., Hasenfratz, A. P., Haug, G. H., Jaccard,
790 S. L., and et al.: Causes of ice age intensification across the Mid-Pleistocene Transition, *Proceedings of the National Academy of Sciences*,
114, 13 114–13 119, <https://doi.org/10.1073/pnas.1702143114>, 2017.
- Clark, P. U. and Pollard, D.: Origin of the Middle Pleistocene Transition by ice sheet erosion of regolith, *Paleoceanography*, 13, 1–9,
<https://doi.org/10.1029/97pa02660>, 1998.



- Colhoun, E. A. and Barrows, T. T.: The Glaciation of Australia, p. 1037–1045, Elsevier, <https://doi.org/10.1016/b978-0-444-53447-7.00074-x>, 2011.
- Corradino, J. I., Pullen, A., Leier, A. L., Barbeau, D. L., Scher, H. D., Weislogel, A., Bruner, A., Leckie, D. A., and Currie, L. D.: Ancestral trans–North American Bell River system recorded in late Oligocene to early Miocene sediments in the Labrador Sea and Canadian Great Plains, *GSA Bulletin*, 134, 130–144, <https://doi.org/10.1130/b35903.1>, 2021.
- Cuffey, K. and Paterson, W. S. B.: *The Physics of Glaciers*, Academic Press, 4 edn., 2010.
- 800 Dalton, A. S., Margold, M., Stokes, C. R., Tarasov, L., Dyke, A. S., Adams, R. S., Allard, S., Arends, H. E., Atkinson, N., Attig, J. W., Barnett, P. J., Barnett, R. L., Batterson, M., Bernatchez, P., Borns, H. W., Breckenridge, A., Briner, J. P., Brouard, E., Campbell, J. E., Carlson, A. E., Clague, J. J., Curry, B. B., Daigneault, R.-A., Dubé-Loubert, H., Easterbrook, D. J., Franzi, D. A., Friedrich, H. G., Funder, S., Gauthier, M. S., Gowan, A. S., Harris, K. L., Héту, B., Hooyer, T. S., Jennings, C. E., Johnson, M. D., Kehew, A. E., Kelley, S. E., Kerr, D., King, E. L., Kjeldsen, K. K., Knaeble, A. R., Lajeunesse, P., Lakeman, T. R., Lamothe, M., Larson, P., Lavoie, M., Loope, H. M.,
- 805 Lowell, T. V., Lusardi, B. A., Manz, L., McMartin, I., Nixon, F. C., Occhietti, S., Parkhill, M. A., Piper, D. J., Pronk, A. G., Richard, P. J., Ridge, J. C., Ross, M., Roy, M., Seaman, A., Shaw, J., Stea, R. R., Teller, J. T., Thompson, W. B., Thorleifson, L. H., Utting, D. J., Veillette, J. J., Ward, B. C., Weddle, T. K., and Wright, H. E.: An updated radiocarbon-based ice margin chronology for the last deglaciation of the North American Ice Sheet Complex, *Quaternary Science Reviews*, 234, 106–223, <https://doi.org/10.1016/j.quascirev.2020.106223>, 2020.
- de Fleurian, B., Werder, M. A., Beyer, S., Brinkerhoff, D. J., Delaney, I., Dow, C. F., Downs, J., Gagliardini, O., Hoffman, M. J., Hooke,
- 810 R. L., Seguinot, J., and Sommers, A. N.: SHMIP The subglacial hydrology model intercomparison Project, *Journal of Glaciology*, 64, 897–916, <https://doi.org/10.1017/jog.2018.78>, 2018.
- Dowdeswell, J. A. and Siegert, M. J.: Ice-sheet numerical modeling and marine geophysical measurements of glacier-derived sedimentation on the Eurasian Arctic continental margins, *Geological Society of America Bulletin*, 111, 1080–1097, [https://doi.org/10.1130/0016-7606\(1999\)111<1080:isnmam>2.3.co;2](https://doi.org/10.1130/0016-7606(1999)111<1080:isnmam>2.3.co;2), 1999.
- 815 Drew, M. and Tarasov, L.: Surging of a Hudson Strait-scale ice stream: subglacial hydrology matters but the process details mostly do not, *The Cryosphere*, 17, 5391–5415, <https://doi.org/10.5194/tc-17-5391-2023>, 2023.
- Drucker, D. C. and Prager, W.: Soil mechanics and plastic analysis or limit design, *Quarterly of Applied Mathematics*, 10, 157–165, <https://doi.org/10.1090/qam/48291>, 1952.
- Dyez, K. A., Hönisch, B., and Schmidt, G. A.: Early Pleistocene Obliquity-Scale pCO₂ Variability at 1.5 Million Years Ago, *Paleoceanography and Paleoclimatology*, 33, 1270–1291, <https://doi.org/10.1029/2018pa003349>, 2018.
- 820 Dyke, A. S.: An outline of North American deglaciation with emphasis on central and northern Canada, *Developments in Quaternary Sciences*, p. 373–424, [https://doi.org/10.1016/s1571-0866\(04\)80209-4](https://doi.org/10.1016/s1571-0866(04)80209-4), 2004.
- Ehlers, T. A., Farley, K. A., Rusmore, M. E., and Woodsworth, G. J.: Apatite (U-Th)/He signal of large-magnitude accelerated glacial erosion, southwest British Columbia, *Geology*, 34, 765, <https://doi.org/10.1130/g22507.1>, 2006.
- 825 Elderfield, H., Ferretti, P., Greaves, M., Crowhurst, S., McCave, I. N., Hodell, D., and Piotrowski, A. M.: Evolution of Ocean Temperature and Ice Volume Through the Mid-Pleistocene Climate Transition, *Science*, 337, 704–709, <https://doi.org/10.1126/science.1221294>, 2012.
- Engelder, J. and Scholz, C.: The role of asperity indentation and ploughing in rock friction—II, *International Journal of Rock Mechanics and Mining Sciences & Geomechanics Abstracts*, 13, 155–163, [https://doi.org/10.1016/0148-9062\(76\)90820-2](https://doi.org/10.1016/0148-9062(76)90820-2), 1976.
- Fenton, M. M., Schreiner, B. T., Nielsen, E., and Pawlowicz, J. G.: *Quaternary Geology of the Western Plains*, Canadian Society of Petroleum
- 830 Geologists and Alberta Research Council, https://static.ags.aer.ca/files/document/Atlas/chapter_26.pdf, 1994.
- Fulton, R. J.: *Surficial materials of Canada*, <https://doi.org/10.4095/205040>, 1995.



- GIS Team National Park Service, A. R. O.: State Surficial Geology Map of Alaska, 1999.
- Goudie, A. S. and Viles, H. A.: Weathering and the global carbon cycle: Geomorphological perspectives, *Earth-Science Reviews*, 113, 59–71, <https://doi.org/10.1016/j.earscirev.2012.03.005>, 2012.
- 835 Group, G. C.: GEBCO 2023 Grid, <https://doi.org/doi:10.5285/f98b053b-0cbc-6c23-e053-6c86abc0af7b>, 2023.
- Gulick, S. P. S., Jaeger, J. M., Mix, A. C., Asahi, H., Bahlburg, H., Belanger, C. L., Berbel, G. B. B., Childress, L., Cowan, E., Drab, L., Forwick, M., Fukumura, A., Ge, S., Gupta, S., Kioka, A., Konno, S., Levay, L. J., Maerz, C., Matsuzaki, K. M., McClymont, E. L., Moy, C., Mueller, J., Nakamura, A., Ojima, T., Ribeiro, F. R., Ridgway, K. D., Romero, O. E., Slagle, A. L., Stoner, J. S., St-Onge, G., Suto, I., Walczak, M. D., Worthington, L. L., Bailey, I., Enkelmann, E., Reece, R., and Swartz, J. M.: Mid-Pleistocene Climate Transition Drives
840 Net Mass Loss From Rapidly Uplifting St. Elias Mountains, Alaska, *PNAS*, 112, 15 042–15 047, 2015.
- Haldorsen, S.: Grain-size distribution of subglacial till and its reation to glacial scrushing and abrasion, *Boreas*, 10, 91–105, <https://doi.org/10.1111/j.1502-3885.1981.tb00472.x>, 2008.
- Hallet, B.: Subglacial Regelation Water Film, *Journal of Glaciology*, 23, 321–334, <https://doi.org/10.1017/s0022143000029932>, 1979.
- Hanna, M. C., Lister, C. J., Kublik, K., King, H. M., Kung, L. E., McCarthy, W. M., McDannell, K. T., and Jassim, Y.: Qualitative
845 petroleum resource assessment of western Hudson Bay, Foxe Channel, and Repulse Bay, Manitoba, Nunavut, Ontario, and Quebec, <https://doi.org/10.4095/311260>, 2018.
- Harbor, J. M., Hallet, B., and Raymond, C. F.: A numerical model of landform development by glacial erosion, *Nature*, 333, 347–349, <https://doi.org/10.1038/333347a0>, 1988.
- Hay, W. W., Shaw, C. A., and Wold, C. N.: Mass-balanced paleogeographic reconstructions, *Geologische Rundschau*, 78, 207–242,
850 <https://doi.org/10.1007/bf01988362>, 1989.
- Hildes, D. H., Clarke, G. K., Flowers, G. E., and Marshall, S. J.: Subglacial erosion and englacial sediment transport modelled for North American ice sheets, *Quaternary Science Reviews*, 23, 409–430, <https://doi.org/10.1016/j.quascirev.2003.06.005>, 2004.
- Hildes, D. H. D.: Modelling subglacial erosion and englacial sediment transport of the North American ice sheets, Ph.D. thesis, University of British Columbia, Department of Earth, Ocean and Atmospheric Sciences Faculty of Science 2020 – 2207 Main Mall Vancouver, BC
855 Canada V6T 1Z4, <https://doi.org/10.14288/1.0052346>, 2001.
- Hönisch, B.: Paleo-CO₂ data archive (Version 1), <https://doi.org/10.5281/zenodo.5777278>, 2021.
- Hönisch, B., Hemming, N. G., Archer, D., Siddall, M., and McManus, J. F.: Atmospheric Carbon Dioxide Concentration Across the Mid-Pleistocene Transition, *Science*, 324, 1551–1554, <https://doi.org/10.1126/science.1171477>, 2009.
- Hooyer, T. S., Cohen, D., and Iverson, N. R.: Control of glacial quarrying by bedrock joints, *Geomorphology*, 153–154, 91–101,
860 <https://doi.org/10.1016/j.geomorph.2012.02.012>, 2012.
- Hubbard, B. and Nienow, P.: Alpine subglacial hydrology, *Quaternary Science Reviews*, 16, 939–955, [https://doi.org/10.1016/s0277-3791\(97\)00031-0](https://doi.org/10.1016/s0277-3791(97)00031-0), 1997.
- Hubbard, B. and Sharp, M.: Basal Ice Fades and Their Formation in the Western Alps, *Arctic and Alpine Research*, 27, 301–310, <https://doi.org/10.1080/00040851.1995.12003127>, 1995.
- 865 Iverson, N. R.: Laboratory Simulations Of Glacial Abrasion: Comparison With Theory, *Journal of Glaciology*, 36, 304–314, <https://doi.org/10.3189/002214390793701264>, 1990.
- Iverson, N. R.: Potential effects of subglacial water-pressure fluctuations on quarrying, *Journal of Glaciology*, 37, 27–36, <https://doi.org/10.3189/s0022143000042763>, 1991.
- Iverson, N. R.: A theory of glacial quarrying for landscape evolution models, *Geology*, 40, 679–682, <https://doi.org/10.1130/g33079.1>, 2012.



- 870 Iverson, N. R. and Semmens, D. J.: Intrusion of ice into porous media by regelation: A mechanism of sediment entrainment by glaciers, *Journal of Geophysical Research: Solid Earth*, 100, 10 219–10 230, <https://doi.org/10.1029/95jb00043>, 1995.
- Iverson, R. M.: A Constitutive Equation for Mass-Movement Behavior, *The Journal of Geology*, 93, 143–160, <https://doi.org/10.1086/628937>, 1985.
- Jauer, C. D. and Budkewitsch, P.: Old marine seismic and new satellite radar data: Petroleum exploration of north west Labrador Sea, Canada, *Marine and Petroleum Geology*, 27, 1379–1394, <https://doi.org/10.1016/j.marpetgeo.2010.03.003>, 2010.
- 875 Jenson, J. W., Clark, P. U., MacAyeal, D. R., Ho, C., and Vela, J. C.: Numerical modeling of advective transport of saturated deforming sediment beneath the Lake Michigan Lobe, Laurentide Ice Sheet, *Geomorphology*, 14, 157–166, [https://doi.org/10.1016/0169-555x\(95\)00056-0](https://doi.org/10.1016/0169-555x(95)00056-0), 1995.
- Jenson, J. W., MacAyeal, D. R., Clark, P. U., Ho, C. L., and Vela, J. C.: Numerical modeling of subglacial sediment deformation: Implications
880 for the behavior of the Lake Michigan Lobe, Laurentide Ice Sheet, *Journal of Geophysical Research: Solid Earth*, 101, 8717–8728, <https://doi.org/10.1029/96jb00169>, 1996.
- Karlstrom, T.: Surficial geology of Alaska: U.S. Geological Survey Miscellaneous Geologic Investigations Map 357, 1964.
- Keller, G. R. and Matile, G. L. D.: Drift thickness of southern Manitoba, Geoscientific Map MAP2021-2, <https://www.gov.mb.ca/iem/info/libmin/MAP2021-2.pdf>, 2021.
- 885 Klassen, R. and Gubins, A.: Glacial history and ice flow dynamics applied to drift prospecting and geochemical exploration, in: *Proceedings of Exploration*, vol. 97, pp. 221–232, 1997.
- Koppes, M. N. and Montgomery, D. R.: The relative efficacy of fluvial and glacial erosion over modern to orogenic timescales, *Nature Geoscience*, 2, 644–647, <https://doi.org/10.1038/ngeo616>, 2009.
- Krabbendam, M. and Glasser, N. F.: Glacial erosion and bedrock properties in NW Scotland: Abrasion and plucking, hardness and joint
890 spacing, *Geomorphology*, 130, 374–383, <https://doi.org/10.1016/j.geomorph.2011.04.022>, 2011.
- Lambeck, K., Rouby, H., Purcell, A., Sun, Y., and Sambridge, M.: Sea level and global ice volumes from the Last Glacial Maximum to the Holocene, *Proceedings of the National Academy of Sciences*, 111, 15 296–15 303, <https://doi.org/10.1073/pnas.1411762111>, 2014.
- Laske, G., Masters, G., Ma, Z., and Pasyanos, M. E.: Update on CRUST1.0: a 1-degree Global Model of Earth’s Crust, in: *Geophysical Research Abstracts*, vol. 15 of *European Geosciences Union General Assembly 2013*, European Geosciences Union, Vienna, Austria,
895 2013.
- Lazeroms, W. M. J., Jenkins, A., Gudmundsson, G. H., and van de Wal, R. S. W.: Modelling present-day basal melt rates for Antarctic ice shelves using a parametrization of buoyant meltwater plumes, *The Cryosphere*, 12, 49–70, <https://doi.org/10.5194/tc-12-49-2018>, 2018.
- Le Morzadec, K., Tarasov, L., Morlighem, M., and Seroussi, H.: A new sub-grid surface mass balance and flux model for continental-scale ice sheet modelling: testing and last glacial cycle, *Geoscientific Model Development*, 8, 3199–3213, <https://doi.org/10.5194/gmd-8-3199-2015>, 2015.
- 900 Lebedeva, M., Fletcher, R., and Brantley, S.: A mathematical model for steady-state regolith production at constant erosion rate, *Earth Surface Processes and Landforms*, 35, 508–524, <https://doi.org/10.1002/esp.1954>, 2010.
- Matero, I., Gregoire, L., Ivanovic, R., Tindall, J., and Haywood, A.: The 8.2 ka cooling event caused by Laurentide ice saddle collapse, *Earth and Planetary Science Letters*, 473, 205–214, <https://doi.org/10.1016/j.epsl.2017.06.011>, 2017.
- 905 McKinley, I. G. and Chapman, N. A.: The impact of subsidence, uplift and erosion on geological repositories for radioactive wastes, *Volcanic and Tectonic Hazard Assessment for Nuclear Facilities*, p. 548–565, <https://doi.org/10.1017/cbo9780511635380.025>, 2009.



- Melanson, A.: Numerical modelling of subglacial erosion and sediment transport and its application to the North American ice sheets over the last glacial cycle, <https://research.library.mun.ca/2370/>, includes bibliographical references (leaves 76-87)., 2012.
- Melanson, A., Bell, T., and Tarasov, L.: Numerical modelling of subglacial erosion and sediment transport and its application to the North American ice sheets over the Last Glacial cycle, *Quaternary Science Reviews*, 68, 154–174, <https://doi.org/10.1016/j.quascirev.2013.02.017>, 2013.
- 910 Naylor, S., Wickert, A. D., Edmonds, D. A., and Yanites, B. J.: Landscape evolution under the southern Laurentide Ice Sheet, *Science Advances*, 7, <https://doi.org/10.1126/sciadv.abj2938>, 2021.
- Parent, M., Ross, M., Howlett, D., and Bédard, K.: 3D model of the Quaternary sediments in the St. Lawrence valley and adjacent regions, southern Quebec and eastern Ontario, <https://doi.org/10.4095/329082>, 2021.
- 915 Pelletier, J. D., Broxton, P. D., Hazenberg, P., Zeng, X., Troch, P. A., Niu, G.-Y., Williams, Z., Brunke, M. A., and Gochis, D.: A gridded global data set of soil, intact regolith, and sedimentary deposit thicknesses for regional and global land surface modeling, *Journal of Advances in Modeling Earth Systems*, 8, 41–65, <https://doi.org/10.1002/2015ms000526>, 2016.
- Pianosi, F. and Wagener, T.: A simple and efficient method for global sensitivity analysis based on cumulative distribution functions, *Environmental Modelling & Software*, 67, 1–11, <https://doi.org/10.1016/j.envsoft.2015.01.004>, 2015.
- 920 Pollard, D. and DeConto, R. M.: Antarctic ice and sediment flux in the Oligocene simulated by a climate–ice sheet–sediment model, *Palaeogeography, Palaeoclimatology, Palaeoecology*, 198, 53–67, [https://doi.org/10.1016/s0031-0182\(03\)00394-8](https://doi.org/10.1016/s0031-0182(03)00394-8), 2003.
- Pollard, D. and DeConto, R. M.: A Coupled Ice-Sheet/Ice-Shelf/Sediment Model Applied to a Marine-Margin Flowline: Forced and Unforced Variations, *Glacial Sedimentary Processes and Products*, pp. 37–52, <https://doi.org/10.1002/9781444304435.ch4>, 2009.
- 925 Pollard, D. and DeConto, R. M.: A simple inverse method for the distribution of basal sliding coefficients under ice sheets, applied to Antarctica, *The Cryosphere*, 6, 953–971, <https://doi.org/10.5194/tc-6-953-2012>, 2012.
- Pollard, D. and DeConto, R. M.: Continuous simulations over the last 40 million years with a coupled Antarctic ice sheet-sediment model, *Palaeogeography, Palaeoclimatology, Palaeoecology*, 537, 109–374, <https://doi.org/10.1016/j.palaeo.2019.109374>, 2020.
- Porter, C., Morin, P., Howat, I., Noh, M.-J., Bates, B., Peterman, K., Keesey, S., Schlenk, M., Gardiner, J., Tomko, K., Willis, M., Kelleher, C., Cloutier, M., Husby, E., Foga, S., Nakamura, H., Platson, M., Wethington, Michael, J., Williamson, C., Bauer, G., Enos, J., Arnold, G., Kramer, W., Becker, P., Doshi, A., D’Souza, C., Cummens, P., Laurier, F., and Bojesen, M.: ArcticDEM, Version 3, <https://doi.org/10.7910/DVN/OHHUKH>, 2018.
- 930 Porter, C., Howat, I., Noh, M.-J., Husby, E., Khuvis, S., Danish, E., Tomko, K., Gardiner, J., Negrete, A., Yadav, B., Klassen, J., Kelleher, C., Cloutier, M., Bakker, J., Enos, J., Arnold, G., Bauer, G., and Morin, P.: ArcticDEM - Mosaics, Version 4.1, <https://doi.org/10.7910/DVN/3VDC4W>, 2023.
- 935 Rohling, E. J., Foster, G. L., Grant, K. M., Marino, G., Roberts, A. P., Tamisiea, M. E., and Williams, F.: Sea-level and deep-sea-temperature variability over the past 5.3 million years, *Nature*, 508, 477–482, <https://doi.org/10.1038/nature13230>, 2014.
- Roy, M., Clark, P. U., Raisbeck, G. M., and Yiou, F.: Geochemical constraints on the regolith hypothesis for the middle Pleistocene transition, *Earth and Planetary Science Letters*, 227, 281–296, <https://doi.org/10.1016/j.epsl.2004.09.001>, 2004.
- 940 Russell, H., Atkinson, N., Bajc, A., Brodaric, B., Keller, G., Lo, K., Parent, M., Pyne, M., Smith, R., and Todd, B.: A 3-D framework of surficial geology for Canada, Joint Annual Meeting, Programs with Abstracts, 40, <https://geoscan.nrcan.gc.ca/starweb/geoscan/servlet.starweb?path=geoscan/fulle.web&search1=R=327036>, 2017.
- Saltelli, A.: Making best use of model evaluations to compute sensitivity indices, *Computer Physics Communications*, 145, 280–297, [https://doi.org/10.1016/s0010-4655\(02\)00280-1](https://doi.org/10.1016/s0010-4655(02)00280-1), 2002.



- 945 Saltelli, A., Ratto, M., Andres, T., Campolongo, F., Cariboni, J., Gatelli, D., Saisana, M., and Tarantola, S.: Global Sensitivity Analysis, John Wiley & Sons, Ltd., The Atrium, Southern Gate, Chichester, West Sussex PO19 8SQ, England, 1 edn., 2008.
- Saltelli, A., Aleksankina, K., Becker, W., Fennell, P., Ferretti, F., Holst, N., Li, S., and Wu, Q.: Why so many published sensitivity analyses are false: A systematic review of sensitivity analysis practices, *Environmental Modelling & Software*, 114, 29–39, <https://doi.org/10.1016/j.envsoft.2019.01.012>, 2019.
- 950 Schoof, C.: Marine ice-sheet dynamics. Part 1. The case of rapid sliding, *Journal of Fluid Mechanics*, 573, 27–55, <https://doi.org/10.1017/s0022112006003570>, 2007.
- Schulzweida, U.: CDO User Guide, <https://doi.org/10.5281/zenodo.10020800>, 2023.
- Sears, J. W. and Beranek, L. P.: The Great Preglacial “Bell River” of North America: Detrital Zircon Evidence for Oligocene–Miocene Fluvial Connections Between the Colorado Plateau and Labrador Sea, *Geoscience Canada*, 49, <https://doi.org/10.12789/geocanj.2022.49.184>, 955 2022.
- Setterholm, D. R. and Morey, G. B.: <https://doi.org/10.3133/b1989h>, 1995.
- Shangguan, W., Hengl, T., Mendes de Jesus, J., Yuan, H., and Dai, Y.: Mapping the global depth to bedrock for land surface modeling, *Journal of Advances in Modeling Earth Systems*, 9, 65–88, <https://doi.org/10.1002/2016ms000686>, 2017.
- Smith, I. R. and Lesk-Winfield, K.: Drift isopach, till isopach, and till facies reconstructions for Northwest Territories and northern Yukon, 960 <https://doi.org/10.4095/261783>, 2010.
- Soller, D. R. and Garrity, C. P.: Quaternary sediment thickness and bedrock topography of the glaciated United States east of the Rocky Mountains, *Scientific Investigations Map*, <https://doi.org/10.3133/sim3392>, 2018.
- Spratt, R. M. and Lisiecki, L. E.: A Late Pleistocene sea level stack, *Climate of the Past*, 12, 1079–1092, <https://doi.org/10.5194/cp-12-1079-2016>, 2016.
- 965 Staiger, J., Gosse, J., Little, E., Utting, D., Finkel, R., Johnson, J., and Fastook, J.: Glacial erosion and sediment dispersion from detrital cosmogenic nuclide analyses of till, *Quaternary Geochronology*, 1, 29–42, <https://doi.org/10.1016/j.quageo.2006.06.009>, 2006.
- Stashin, S.: Late Cenozoic Basin Evolution of the western Canadian Arctic Archipelago: The Beaufort Formation and Iperk Sequence, Masters thesis, Dalhousie University, <http://hdl.handle.net/10222/80367>, 2021.
- Straume, E. O., Gaina, C., Medvedev, S., Hochmuth, K., Gohl, K., Whittaker, J. M., Abdul Fattah, R., Doornenbal, J. C., and Hopper, 970 J. R.: GlobSed: Updated Total Sediment Thickness in the World’s Oceans, *Geochemistry, Geophysics, Geosystems*, 20, 1756–1772, <https://doi.org/10.1029/2018gc008115>, 2019.
- Tarasov, L. and Peltier, W.: A geophysically constrained large ensemble analysis of the deglacial history of the North American ice-sheet complex, *Quaternary Science Reviews*, 23, 359–388, <https://doi.org/10.1016/j.quascirev.2003.08.004>, 2004.
- Tarasov, L. and Peltier, W.: A calibrated deglacial drainage chronology for the North American continent: evidence of an Arctic trigger for 975 the Younger Dryas, *Quaternary Science Reviews*, 25, 659–688, <https://doi.org/10.1016/j.quascirev.2005.12.006>, 2006.
- Tarasov, L. and Peltier, W. R.: A high-resolution model of the 100 ka ice-age cycle, *Annals of Glaciology*, 25, 58–65, <https://doi.org/10.3189/s026030550001380x>, 1997.
- Tarasov, L. and Peltier, W. R.: Coevolution of continental ice cover and permafrost extent over the last glacial-interglacial cycle in North America, *Journal of Geophysical Research*, 112, <https://doi.org/10.1029/2006jf000661>, 2007.
- 980 Tarasov, L., Dyke, A. S., Neal, R. M., and Peltier, W.: A data-calibrated distribution of deglacial chronologies for the North American ice complex from glaciological modeling, *Earth and Planetary Science Letters*, 315–316, 30–40, <https://doi.org/10.1016/j.epsl.2011.09.010>, 2012.



- Taylor, A.: Sediment thickness map of continental Canada and Canada-U.S. transboundary watersheds, 2023.
- 985 Thomas, E. R., Wolff, E. W., Mulvaney, R., Steffensen, J. P., Johnsen, S. J., Arrowsmith, C., White, J. W., Vaughn, B., and Popp, T.: The 8.2ka event from Greenland ice cores, *Quaternary Science Reviews*, 26, 70–81, <https://doi.org/10.1016/j.quascirev.2006.07.017>, 2007.
- Ugelvig, S. V. and Egholm, D. L.: The influence of basal-ice debris on patterns and rates of glacial erosion, *Earth and Planetary Science Letters*, 490, 110–121, <https://doi.org/10.1016/j.epsl.2018.03.022>, 2018.
- Ugelvig, S. V., Egholm, D. L., and Iverson, N. R.: Glacial landscape evolution by subglacial quarrying: A multiscale computational approach, *Journal of Geophysical Research: Earth Surface*, 121, 2042–2068, <https://doi.org/10.1002/2016jf003960>, 2016.
- 990 Von Mises, R.: *Mechanik der festen Körper im plastisch- deformablen Zustand*, Nachrichten von der Gesellschaft der Wissenschaften zu Göttingen, Mathematisch-Physikalische Klasse, 1913, 582–592, <http://eudml.org/doc/58894>, 1913.
- Weertman, J.: On the Sliding of Glaciers, *Journal of Glaciology*, 3, 33–38, <https://doi.org/10.3189/s0022143000024709>, 1957.
- White, W. A.: Deep Erosion by Continental Ice Sheets, *Geological Society of America Bulletin*, 83, 1037, [https://doi.org/10.1130/0016-7606\(1972\)83\[1037:debcis\]2.0.co;2](https://doi.org/10.1130/0016-7606(1972)83[1037:debcis]2.0.co;2), 1972.
- 995 Wilford, J., Searle, R., Thomas, M., Pagendam, D., and Grundy, M.: A regolith depth map of the Australian continent, *Geoderma*, 266, 1–13, <https://doi.org/10.1016/j.geoderma.2015.11.033>, 2016.
- Willeit, M., Ganopolski, A., Calov, R., Robinson, A., and Maslin, M.: The role of CO₂ decline for the onset of Northern Hemisphere glaciation, *Quaternary Science Reviews*, 119, 22–34, <https://doi.org/10.1016/j.quascirev.2015.04.015>, 2015.
- Willeit, M., Ganopolski, A., Calov, R., and Brovkin, V.: Mid-Pleistocene transition in glacial cycles explained by declining CO₂ and regolith
1000 removal, *Science Advances*, 5, eaav7337, <https://doi.org/10.1126/sciadv.aav7337>, 2019.
- Yokoyama, Y., Esat, T. M., Thompson, W. G., Thomas, A. L., Webster, J. M., Miyairi, Y., Sawada, C., Aze, T., Matsuzaki, H., Okuno, J., Fallon, S., Braga, J.-C., Humblet, M., Iryu, Y., Potts, D. C., Fujita, K., Suzuki, A., and Kan, H.: Rapid glaciation and a two-step sea level plunge into the Last Glacial Maximum, *Nature*, 559, 603–607, <https://doi.org/10.1038/s41586-018-0335-4>, 2018.